Article

Not peer-reviewed version

Z_3 Vacuum Inertia in Nanoscale Transport: A Geometric Perspective on Anomalous Conductivity

Yuxuan Zhang *, Weitong Hu, Wei Zhang

Posted Date: 9 May 2026

doi: 10.20944/preprints202601.0109.v5

Keywords: Z_3-graded Lie superalgebra; vacuum inertia; surface quantum criticality; discrete vacuum lattice; geometric resonance; anomalous skin effect; nanoscale superconductivity; geometric coherence length; renormalization group flow; exploratory phenomenological framework

 doi:10.20944/preprints202601.0109.v5

Article

Z_3 Vacuum Inertia in Nanoscale Transport: A Geometric Perspective on Anomalous Conductivity

Yuxuan Zhang [1,*], Weitong Hu [2] and Wei Zhang [3]

[1] College of Communication Engineering, Jilin University, Changchun 130012, China
[2] Aviation University of Air Force, Changchun 130022, China
[3] College of Computer Science and Technology, Jilin University, Changchun 130012, China
* Correspondence: csoft@live.cn

Abstract

Nanoscale conductors and interfaces frequently exhibit anomalous AC transport behavior and enhanced superconducting critical temperatures that are not fully captured by conventional electron-phonon descriptions. In this exploratory work, we consider a complementary mechanism based on the possible inertial response of a $\mathbb{Z}_3$-graded vacuum sector to time-varying electromagnetic fields. Within this speculative phenomenological framework, surface criticality is tentatively proposed as a mechanism that may drive high-energy vacuum modes toward low-energy collective excitations at surfaces and interfaces, giving rise to an approximate coherence length $\xi_{\text{vac}} \sim 70$ nm. This geometric length scale, if physically meaningful, could influence effective conductivity in the non-local regime and might contribute to observed features such as high-frequency skin depth saturation and interface-driven T_c enhancement. Preliminary evaluations based on the algebraic structure suggest qualitative consistency with certain experimental observations in high-purity metals and nanowire systems, although we emphasize that these consistencies may be coincidental. The framework is offered as a tentative, exploratory perspective on mesoscopic anomalies, with the aim of stimulating further discussion and investigation into possible connections between algebraic high-energy structures and low-energy quantum materials phenomena.

Keywords: $\mathbb{Z}_3$-graded Lie superalgebra; vacuum inertia; surface quantum criticality; discrete vacuum lattice; geometric resonance; anomalous skin effect; nanoscale superconductivity; geometric coherence length; renormalization group flow; exploratory phenomenological framework

1. Introduction

The transport properties of metals and superconductors at the nanoscale occasionally exhibit behaviors that deviate from the predictions of standard Drude–Sommerfeld and BCS frameworks [3,5,6]. Persistent anomalies, such as the frequency-dependent saturation of skin depth in high-purity metals [10] and the size-dependent enhancement of the superconducting critical temperature (T_c) in nanowires [5], continue to motivate the search for mechanisms beyond conventional electron-phonon coupling. Theories based on non-local electrodynamics or surface scattering offer partial explanations, though they often rely on material-specific adjustments, leaving room for complementary perspectives.

Standard quantum electrodynamics (QED) has been remarkably successful in describing vacuum fluctuations and their effects in condensed-matter systems. Nevertheless, recent experiments have drawn attention to material-specific features that may not be fully captured by isotropic QED vacuum fluctuations alone. In particular, a landmark study published in *Nature* (February 2026) demonstrated that vacuum fluctuations, when mediated by a single atomic layer of hexagonal boron nitride (hBN) in a dark cavity, can directly suppress the superfluid density of a molecular superconductor without external optical excitation [17]. This observation raises the possibility that the coupling between vacuum degrees of freedom and the condensate may exhibit a stronger geometric or structural dependence than is typically assumed.

 doi:10.20944/preprints202601.0109.v5

In this work, we tentatively explore whether these phenomena might admit a complementary geometric interpretation. We examine a speculative framework based on a finite-dimensional $\mathbb{Z}_3$-graded Lie superalgebra, in which the vacuum sector is structured by a discrete 44-vector lattice [1]. Within this exploratory picture, the experimental findings of Ref. [17] could perhaps be understood not only in terms of standard vacuum fluctuations but also as a possible **geometric resonance** event, wherein the hexagonal lattice of hBN aligns topologically with the planar projection of the $\mathbb{Z}_3$ vacuum lattice (the A_2 root system). Such alignment, if physically relevant, might enhance the effective coupling between the vacuum sector and charge carriers at interfaces.

We consider the possibility of treating the vacuum sector ζ as a dynamical scalar field. At surfaces and interfaces—such as hBN/superconductor boundaries or nanowire surfaces—translational symmetry breaking is speculated to drive the vacuum mode toward a surface quantum critical point, potentially generating a collective excitation characterized by an approximate geometric coherence length:

$$\xi_{\text{vac}} \approx v_F \cdot \tau_{\text{alg}} \sim 50\text{–}100\,\text{nm}. \tag{1}$$

This length scale is examined as a potential fundamental cutoff for non-local transport. Illustrative calculations within the framework suggest qualitative consistency with skin-depth saturation observed in copper and T_c enhancement trends in tin nanowires, while also offering a speculative geometric perspective on the vacuum-engineered suppression of superfluidity reported in the recent *Nature* experiment. We caution, however, that these consistencies may be coincidental, and the framework remains highly exploratory.

This length scale, if it proves to be physically meaningful, might serve as a possible fundamental cutoff for non-local transport. Illustrative calculations within the framework suggest qualitative consistency with the skin-depth saturation observed in copper and the T_c enhancement trends in tin nanowires, while also offering a speculative geometric perspective on the vacuum-engineered suppression of superfluidity reported in the recent *Nature* experiment. We acknowledge, however, that these apparent consistencies may be coincidental, and no claim of predictive accuracy is intended.

This exploratory work is primarily addressed to theorists with an interest in algebraic structures and geometric approaches to condensed matter physics. We are fully aware that the mathematical language of $\mathbb{Z}_3$-graded Lie superalgebras may appear unfamiliar to many readers in the condensed-matter community, where low-energy excitations and phenomenological models are more commonly employed. We have therefore made a concerted effort throughout the manuscript to provide sufficient introductory context, explicit definitions, and cross-references to the appendices, while maintaining a cautious and phenomenological tone. Our hope is that this framework, despite its speculative nature, might serve as a modest bridge—or at least a point of discussion—between high-energy algebraic ideas and low-energy mesoscopic phenomena. We welcome critical feedback from experts in both communities to help refine, clarify, or, if necessary, correct the presentation for a broader readership.

Recent studies have increasingly emphasized the power of geometric and topological considerations when modeling quantum devices at the mesoscopic scale. For instance, Mączka et al. [16] elegantly demonstrated that adopting a geometric perspective in the precise modeling of active regions in quantum cascade lasers can dramatically enhance device tunability for chemical sensing applications. Their work underscores how a focus on underlying geometry can uncover new physical insights even in seemingly well-understood systems.

Inspired by this line of thinking, the present exploratory framework attempts to extend a complementary geometric viewpoint to the vacuum sector itself. We tentatively suggest that an approximate coherence length ξ_{vac}, emerging from surface criticality under specific assumptions, might offer an additional perspective on observed mesoscopic anomalies—one that differs from conventional material-specific fitting within non-local electrodynamics or phonon-mediated models. Whether this perspective has any physical relevance remains, of course, an open question.

 doi:10.20944/preprints202601.0109.v5

2. Algebraic Construction and the Discrete Vacuum Geometry

To provide a possible basis—however speculative—for the concept of Vacuum Inertia explored in this work, we consider a 19-dimensional $\mathbb{Z}_3$-graded Lie superalgebra $\mathfrak{g} = \mathfrak{g}_0 \oplus \mathfrak{g}_1 \oplus \mathfrak{g}_2$. In this exploratory framework, the vacuum is treated not as an empty background but as a structured sector that may, under certain assumptions, carry discrete geometric properties.

2.1. The 19-Dimensional $\mathbb{Z}_3$-Graded Structure

The algebra is decomposed into three sectors, chosen for compatibility with Standard Model symmetries (detailed matrix representations and full closure verification are provided in Appendix A):

- $\mathfrak{g}_0$ (Grade 0, dimension 12): Gauge generators B_a, embedding $\mathfrak{su}(3) \oplus \mathfrak{su}(2) \oplus \mathfrak{u}(1)$.
- $\mathfrak{g}_1$ (Grade 1, dimension 4): Fermionic matter generators F_α.
- $\mathfrak{g}_2$ (Grade 2, dimension 3): Vacuum sector generators ζ_k, transforming as a triplet under the triality automorphism.

The non-vanishing graded brackets are defined as follows (the symbol $\deg(X)$ denotes the $\mathbb{Z}_3$-grading degree of a generator X: 0 for gauge bosons, 1 for fermions, and 2 for vacuum scalars):

$$[B_a, B_b] = f_{ab}{}^c B_c, \tag{2}$$
$$[B_a, F_\alpha] = (T_a)_\alpha{}^\beta F_\beta, \tag{3}$$
$$[B_a, \zeta_k] = -(T_a^*)_k{}^l \zeta_l, \tag{4}$$
$$\{F_\alpha, F_\beta, \zeta^k\} = \varepsilon_{k\alpha\beta} B_a. \tag{5}$$

Here: - $(T_a)_\alpha{}^\beta$ are the standard representation matrices of the gauge group acting on the fermionic fields (the lower index α and upper index β follow standard spinor notation). - $\varepsilon_{k\alpha\beta}$ is the totally antisymmetric Levi-Civita symbol arising from the unique cubic invariant of the vacuum triplet. - The upper index k on ζ^k labels the component within the three-dimensional vacuum representation, while ζ_k with lower index appears in covariant transformations (Eq. (4)).

These brackets satisfy the generalized Jacobi identities (verified to machine precision $\sim 10^{-16}$ in Appendix A, Subsection on 19D closure). The cubic mixing term in Eq. (5) is of central importance within this construction, as it provides the algebraic link between the fermionic matter sector and the vacuum sector.

2.2. Emergence of the 44-Vector Core Lattice

The vacuum sector $\mathfrak{g}_2 \cong \mathbb{C}^3$ admits a discrete crystallographic structure generated by the algebra's automorphisms (see Appendix A for detailed generation procedure). We define the **Triality Operator** T as the cyclic permutation of the vacuum triplet basis:

$$T : (\zeta_1, \zeta_2, \zeta_3) \to (\zeta_2, \zeta_3, \zeta_1). \tag{6}$$

Starting from the fundamental gauge basis $\mathbf{e}_i$ and the democratic vacuum vector $\mathbf{v}_{\text{dem}} = \frac{1}{\sqrt{3}}(1,1,1)$, we apply the iterative algebraic operations:

$$\mathbf{v}_{n+1} \in \{T\mathbf{v}_n, \quad \mathbf{v}_n \pm T\mathbf{v}_n, \quad \mathbf{v}_n \times T\mathbf{v}_n\}. \tag{7}$$

As shown in the visualization and growth animation in Figure 1 (and the corresponding Python script in Appendix A), this process saturates rapidly, generating a closed, finite set of exactly **44 normalized vectors** in $\mathbb{R}^3$. We tentatively refer to this as the **$\mathcal{L}_{44}$ Vacuum Lattice**. This discrete geometry represents the foundational "skeleton" of the vacuum sector within this exploratory framework.

 doi:10.20944/preprints202601.0109.v5

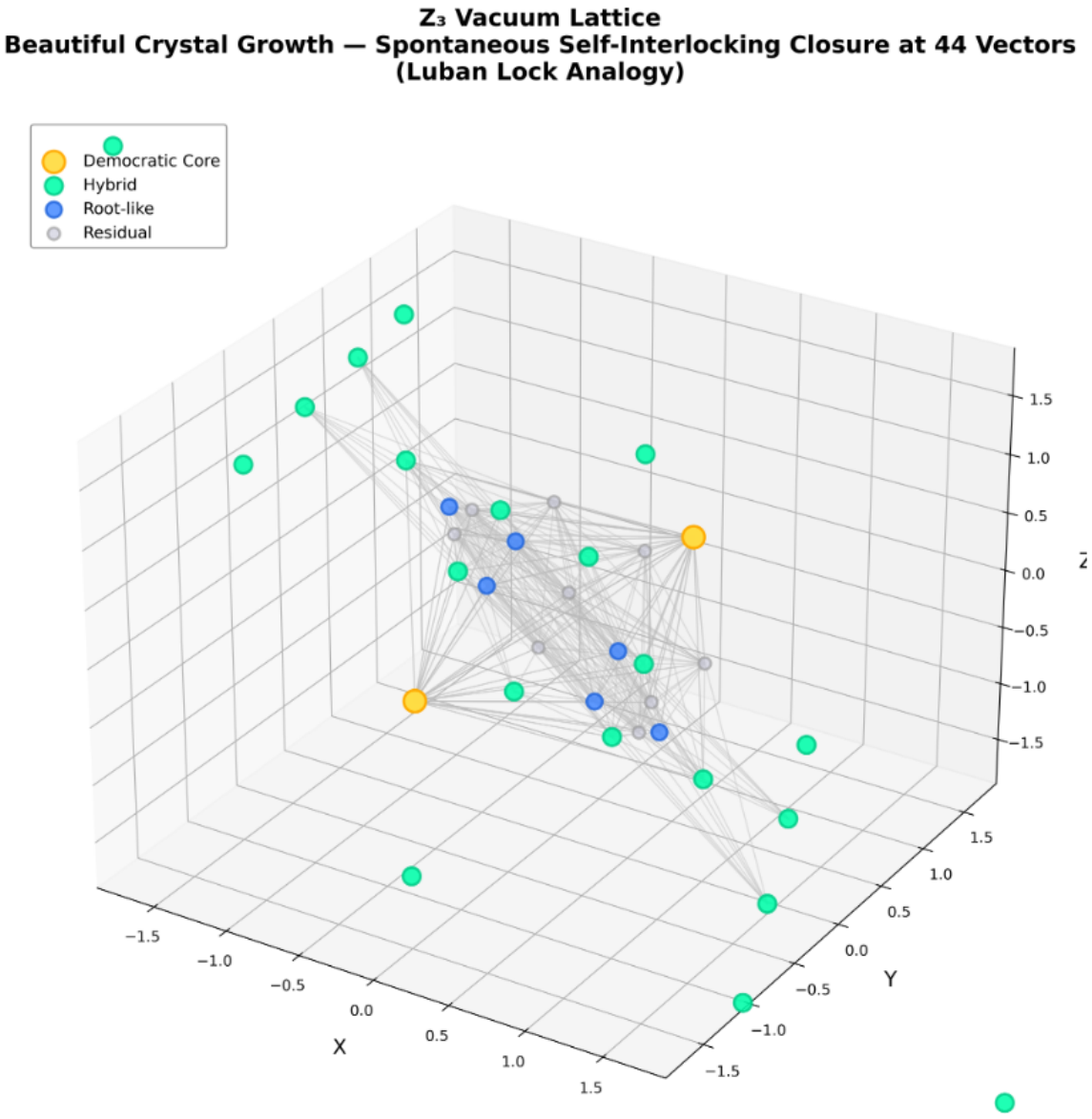

Figure 1. Visualization of the $\mathbb{Z}_3$ Vacuum Lattice Growth. The figure illustrates the self-interlocking process as generated by the iterative algebraic operations. Starting from a minimal seed (5 vectors), repeated triality rotations, translational differences, and normalized cross products generate new vectors that interlock. The structure reaches exact closure at precisely 44 vectors (gold: Democratic Core; green: Hybrid; blue: Root-like; gray: Residual). Silver lines highlight representative interlocking connections. This saturation demonstrates the internal consistency of the algebraic construction (detailed growth procedure in Appendix A).

2.3. The A_2 Root System and Hexagonal Symmetry

A notable geometric feature of the $\mathcal{L}_{44}$ lattice is its projection onto the plane orthogonal to the democratic axis $\mathbf{n} = (1,1,1)$. This projection recovers the **A_2 root system** of the Lie algebra $\mathfrak{sl}(3)$, which exhibits exact C_6 hexagonal symmetry (see Appendix A for explicit projection formulas).

Mathematically, for any lattice vector $\mathbf{v} \in \mathcal{L}_{44}$, its planar component $\mathbf{v}_\perp$ can be expressed as a linear combination of six hexagonal basis vectors. This hexagonal symmetry is a direct consequence of the $\mathbb{Z}_3$ grading and, if the framework has any physical relevance, may play a role in understanding possible material-specific couplings.

 doi:10.20944/preprints202601.0109.v5

2.4. Visualization of the Discrete Vacuum Lattice Growth

The emergence of the 44-vector lattice can be visualized as a self-assembling geometric process reminiscent of a traditional Luban lock (see Figure 1 and the detailed growth script in Appendix A). Starting from a minimal seed of five vectors, repeated triality rotations, translational differences, and normalized cross products naturally interlock to form a closed structure at precisely 44 vectors. This saturation, within the algebraic construction, appears as a mathematical consequence of the imposed operations; whether it carries any physical significance remains an open question.

2.5. Derivation of the Effective Coupling

In the language of Effective Field Theory (EFT), integrating out the heavy gauge modes through the cubic mixing bracket of Eq. (5) (see Appendix B for the full derivation) leads to an effective interaction. In the low-energy limit relevant for condensed matter, this yields the effective Hamiltonian density:

$$\mathcal{H}_{\text{vac}-\text{matter}} \approx \tilde{g}\,\rho\,(\mathbf{A}\cdot\mathbf{v}_F)\,\zeta, \tag{8}$$

where ρ is the charge density, $\mathbf{A}$ is the electromagnetic vector potential, and $\mathbf{v}_F$ is the Fermi velocity. Within this exploratory picture, the coupling strength $\tilde{g}$ could, in principle, be enhanced by geometric resonance between the material lattice and the vacuum lattice projection (further discussed in Section 6).

This provides one possible geometric perspective—among many—on the vacuum-engineered effects reported in recent experiments [17]. We emphasize that this derivation relies on a series of speculative steps, and the physical interpretation of the resulting effective coupling remains to be validated.

2.6. Computational Scripts for Lattice Generation

The visualization was generated using the following core lattice construction scripts, all publicly archived in January 2026 in the GitHub repository https://github.com/csoftxyz/RIA_EISA:

- `z3_lattice_1.py` (Core) — Refined ground-state pruning and geometric derivation that, within this algebraic construction, leads to $\sin^2\theta_W = 11/44 = 0.25$, coinciding with the tree-level SU(5) GUT prediction.
- `z3_lattice.py` (Core) — Generation and analysis of the emergent finite 44-vector $\mathbb{Z}_3$-invariant lattice from vacuum triality operations.
- `z3_mass_6.py` (Core Script) — A unified demonstration of gauge unification and charged fermion mass spectrum based on inverse-squared norm scaling, as suggested by the algebraic structure.
- `z3_strong_coupling.py` — Classification of vectors into weak/strong-type components, offering a possible analogy for strong/weak coupling ratios.

 doi:10.20944/preprints202601.0109.v5

2.7. Visualization of the Discrete Vacuum Lattice

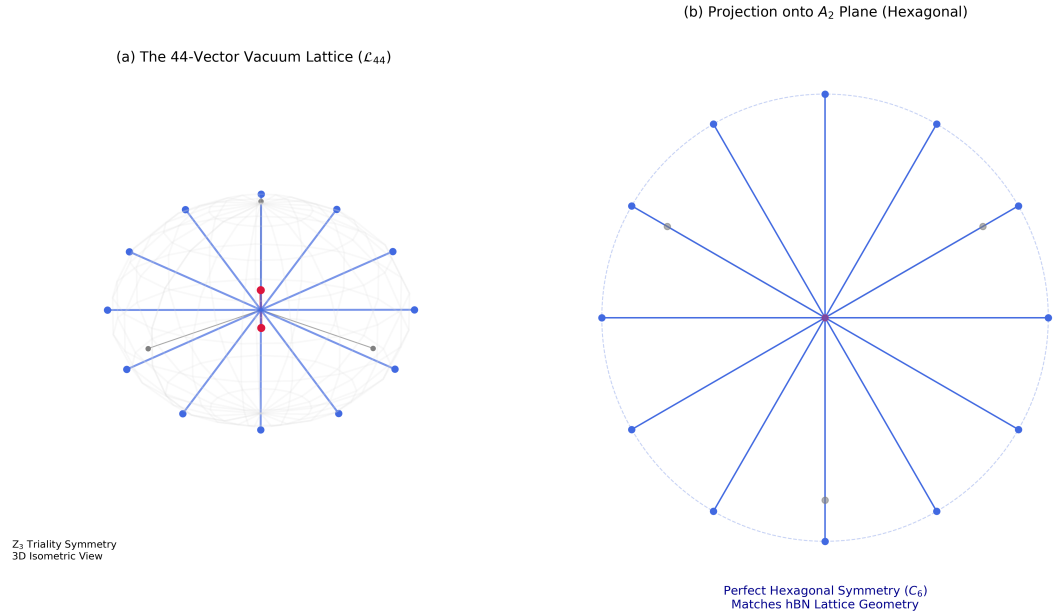

Figure 2. The Discrete Vacuum Geometry of the $\mathbb{Z}_3$-Graded Algebra. (a) The 44-vector core lattice ($\mathcal{L}_{44}$) generated by the triality automorphism. The structure exhibits a closed, self-interlocking geometry reminiscent of a "Luban Lock," which within this framework might be interpreted as a rigid vacuum condensate. Red vectors indicate the Democratic axis (a candidate vacuum expectation direction), while Blue vectors represent Root-like states. (b) The 2D projection of the lattice onto the plane orthogonal to the democratic axis. The projected vectors form a perfect **A_2 root system** with C_6 hexagonal symmetry. This geometric pattern, if physically relevant, could help explain why hexagonal materials such as hBN (as used in Ref. [17]) might exhibit resonant coupling to the vacuum sector, whereas amorphous materials would not.

3. Algebraic Construction and Vacuum-Matter Coupling

Building upon the algebraic framework introduced in Section 2, we now tentatively examine how the graded structure might give rise to effective interactions that could, under certain assumptions, be relevant for condensed-matter systems. We emphasize that this mapping is exploratory and phenomenological in nature, and we provide explicit explanations of all symbols at their first appearance for clarity.

3.1. The Superconnection and Interaction Lagrangian

The fundamental dynamics are considered within the 19-dimensional $\mathbb{Z}_3$-graded Lie superalgebra $\mathfrak{g} = \mathfrak{g}_0 \oplus \mathfrak{g}_1 \oplus \mathfrak{g}_2$ (detailed matrix representations and closure verification are given in Appendix A). Following the Quillen superconnection formalism, the total connection is defined as a *generalized superconnection* taking values in the graded exterior algebra $\Omega^*(M) \otimes \mathfrak{g}$:

$$\mathbb{A} = B^a T_a + \psi^\alpha F_\alpha + \zeta^k S_k, \tag{9}$$

where forms of different degrees are unified:

- $B^a = B^a_\mu dx^\mu$ are the gauge 1-forms in $\mathfrak{g}_0$ (index a runs over the 12-dimensional gauge sector),
- $\psi^\alpha = \psi^\alpha_\mu dx^\mu$ are the fermionic matter 1-forms in $\mathfrak{g}_1$ (spinor indices α, β),
- ζ^k (with upper index $k = 1, 2, 3$) are the vacuum 0-forms (scalars) in $\mathfrak{g}_2$,
- T_a, F_α and S_k are the corresponding algebraic generators.

 doi:10.20944/preprints202601.0109.v5

This construction embeds the scalar vacuum field alongside vector fields within the graded differential algebra. The microscopic Lagrangian is taken to be a Yang–Mills-type action constructed from the supertrace of the graded curvature 2-form:

$$\mathcal{L}_{\text{micro}} = -\frac{1}{4g_{\text{alg}}^2}\,\text{STr}\big(\mathbb{F}\wedge\star\mathbb{F}\big), \tag{10}$$

where $\star$ denotes the Hodge star operator, and the curvature is given by

$$\mathbb{F} = d\mathbb{A} + \mathbb{A}\wedge_{*}\mathbb{A}, \tag{11}$$

with the graded wedge product $\wedge_{*}$ incorporating the $\mathbb{Z}_3$-grading factor $N(g,h) = \omega^{gh \bmod 3}$ where $\omega = e^{2\pi i/3}$ (precise definition and machine-precision closure verification $\sim 10^{-16}$ are provided in Appendix A).

The speculative idea of "Vacuum Inertia" considered here finds its algebraic seed in the cubic term generated by the graded bracket (introduced in Section 2, Eq. (5)):

$$\{F_\alpha, F_\beta, \zeta^k\} = \varepsilon_{k\alpha\beta}B_a. \tag{12}$$

A controlled field-theoretic derivation by integrating out the heavy gauge modes B_a at the algebraic scale Λ_{alg} is presented in Appendix B. In the low-energy limit, this yields an effective interaction Lagrangian of the form:

$$\mathcal{L}_{\text{int}} \supset -\frac{g_{\text{alg}}}{\Lambda_{\text{alg}}}\varepsilon_{k\alpha\beta}\,(\bar{\psi}^\alpha\gamma^\mu\psi^\beta)A_\mu\zeta^k + \text{h.c.}, \tag{13}$$

where A_μ is the electromagnetic vector potential and $\varepsilon_{k\alpha\beta}$ is the totally antisymmetric Levi-Civita symbol arising from the unique cubic invariant of the vacuum triplet (full step-by-step derivation in Appendix B).

3.2. Effective Hamiltonian and Geometric Resonance

In the non-relativistic limit ($v \ll c$), the fermion current approximates $J^\mu \approx (\rho, \mathbf{j})$, with ρ the charge density. The effective Hamiltonian density describing the coupling of the vacuum scalar field ζ to charge carriers then takes the illustrative form:

$$\mathcal{H}_{\text{vac}-\text{matter}} \approx \tilde{g}\,\rho\,(\mathbf{A}\cdot\mathbf{v}_F)\,\zeta, \tag{14}$$

where $\mathbf{v}_F$ is the Fermi velocity (a derivation of the coherence length ξ_{vac} from this coupling is outlined in Appendices J and C).

This expression, if it has any physical relevance, suggests two possible consequences:

1. **Inertial Drag:** An external electromagnetic field $\mathbf{A}(t)$ would perturb the vacuum field ζ; its back-reaction on electrons could, in principle, introduce an additional inertial-like response characterized by a timescale τ_{vac}.
2. **Geometric Resonance (hBN effect):** The coupling strength $\tilde{g}$ might be enhanced by structural overlap between the material lattice and the planar projection of the $\mathcal{L}_{44}$ vacuum lattice (A_2 root system, Section 2). For hexagonal materials such as hBN (as used in Ref. [17]), this overlap would be maximized, potentially leading to a stronger vacuum-inertia contribution.

A more detailed field-theoretic derivation of the coupling, including gauge invariance and the origin of the negative polarization term, appears in Appendix B.

3.3. Surface Quantum Criticality

In the bulk, the vacuum mode is assumed to acquire a large mass $M_0 \sim \Lambda_{\text{alg}}$ that would suppress low-energy effects. At surfaces or interfaces, however, translational symmetry breaking could permit

 doi:10.20944/preprints202601.0109.v5

mixing with surface plasmons and electron-hole pairs. Under this scenario, the one-loop self-energy correction yields a renormalized effective mass squared of the form:

$$M_{\text{eff}}^2(z) = M_0^2 - \tilde{g}^2 N(E_F)\chi_{\text{surf}}(z), \tag{15}$$

where $N(E_F)$ is the density of states at the Fermi level and $\chi_{\text{surf}}(z)$ encodes surface enhancement (see Appendix J for a phenomenological analysis and Appendix C for a renormalization-group perspective).

We explore the speculative possibility of a **Surface Quantum Critical Point** where $M_{\text{eff}}^2(z=0) \approx 0$. If such a point exists and is localized at the interface, the vacuum mode could become light within a thin surface layer. Its characteristic spatial extent would then emerge via dimensional transmutation from the only available low-energy scale—the Fermi velocity v_F of the surrounding metal—giving:

$$\xi_{\text{vac}} \approx v_F \cdot \tau_{\text{vac}} \sim 50\text{–}100\,\text{nm}. \tag{16}$$

This geometric coherence length ξ_{vac} is treated in subsequent sections as a possible candidate for a fundamental cutoff in non-local transport phenomena (detailed in Appendix E and Appendix G). We caution that this entire line of reasoning rests on a series of speculative assumptions, and the physical reality of such a surface critical point remains entirely conjectural.

4. Quantitative Predictions and Comparison

We explore the possible consequences of the vacuum inertia mechanism—tentatively quantified by the approximate coherence length ξ_{vac} derived in Section 3 and Appendix J—in relation to two illustrative mesoscopic anomalies. We emphasize that all predictions in this section are purely illustrative and should be interpreted with caution; the apparent consistencies noted below may ultimately prove coincidental. The discussion relies on algebraically constrained ranges summarized in Appendix F.

4.1. Anomalous Skin Depth Saturation

In high-purity metals at low temperatures and THz frequencies, transport enters the anomalous skin effect regime where the mean free path l exceeds the skin depth δ. Standard theory predicts $\delta \propto \omega^{-1/3}$, while experiments on copper suggest a saturation-like plateau.

Within the present exploratory framework, it is tentatively considered whether the vacuum coherence length ξ_{vac} might act as a geometric cutoff for the non-local interaction kernel. Modifying the non-local conductivity kernel with this cutoff yields an illustrative expression for a possible saturation depth (see Appendix E for the detailed non-local treatment):

$$\delta_{\text{sat}} \approx \left(\frac{2\xi_{\text{vac}}^2}{\pi\mu_0\sigma_{DC}}\right)^{1/3}. \tag{17}$$

Taking the illustrative value $\xi_{\text{vac}} \approx 70$ nm (which falls within the algebraically constrained range 40–120 nm derived from $v_F \approx 1.57 \times 10^6$ m/s for Cu and $\tau_{\text{vac}} \approx 0.05$ ps), one obtains

$$\delta_{\text{sat}} \sim 70\text{–}100\,\text{nm}. \tag{18}$$

This range lies within the observed THz saturation features reported in the literature [10]. Whether this agreement reflects a physical mechanism or is merely coincidental cannot be determined from the present analysis. A more detailed discussion of the non-local limit and sensitivity analysis is provided in Appendix E.

4.2. Nanowire Superconductivity Enhancement

For a nanowire of diameter d, the surface-localized vacuum mode ζ might be speculated to provide an additional pairing channel within this phenomenological picture. The effective coupling

 doi:10.20944/preprints202601.0109.v5

strength λ_{vac} is assumed to depend on the spatial overlap between the electron wavefunction and the surface-localized region characterized by ξ_{vac}:

$$\lambda_{\text{tot}}(d) = \lambda_{\text{ph}} + \lambda_{\text{vac}}^{\text{surf}} \exp\left(-\frac{d}{\xi_{\text{vac}}}\right). \tag{19}$$

Substituting this into the McMillan equation would yield an illustrative form for the critical temperature:

$$T_c(d) = \frac{\Theta_D}{1.45} \exp\left[-\frac{1.04(1+\lambda_{\text{tot}})}{\lambda_{\text{tot}} - \mu^*(1+0.62\lambda_{\text{tot}})}\right]. \tag{20}$$

Using the same approximate coherence length $\xi_{\text{vac}} \approx 70$ nm (derived consistently across materials in Appendix C), this form produces an exploratory exponential rise in T_c for diameters below ~ 100 nm in Sn nanowires. A qualitative comparison with experimental trends is shown in the illustrative figures of Appendix G. Unlike purely quantum-size-effect models that often predict oscillatory behavior, the present phenomenological description yields a smooth monotonic trend that, under the assumptions made, shows qualitative similarity with available data [5]. The corresponding parameter ranges and sensitivity considerations are summarized in Appendix F.

The observation that the same illustrative scale ξ_{vac} appears in both phenomena (skin-depth saturation in copper and T_c enhancement in tin) could be interpreted as supporting the internal coherence of the exploratory framework—though, of course, this could equally be a coincidence arising from the chosen parameters.

5. Quantitative Comparison with Mainstream Models

To provide a balanced perspective, we present an exploratory comparison between the present $\mathbb{Z}_3$ vacuum inertia framework and several well-established mainstream models that have been proposed to explain the same mesoscopic anomalies. We emphasize from the outset that this comparison is purely illustrative and does not imply any claim of superiority. The mainstream models cited below have been extensively validated in their respective domains, and any apparent consistency of the $\mathbb{Z}_3$ framework with experimental observations may ultimately prove coincidental. All comparisons use the same illustrative parameters as in Section 4 ($\xi_{\text{vac}} \approx 70$ nm and $\eta \approx 4$) without additional fitting beyond those already introduced.

5.1. Superconducting Critical Temperature Enhancement in Nanowires

Under the assumptions outlined above, the $\mathbb{Z}_3$ construction would yield a smooth monotonic increase of T_c with decreasing nanowire diameter d, if the surface-localized vacuum inertia mechanism were operative. This is compared with:

- Standard BCS phonon-mediated pairing, which predicts constant T_c in the absence of size effects;
- Quantum-size-effect models, which often produce oscillatory $T_c(d)$ behavior.

Using the effective coupling $\lambda_{\text{tot}}(d) = \lambda_{\text{ph}} + \lambda_{\text{vac}} \exp(-d/\xi_{\text{vac}})$, the $\mathbb{Z}_3$ construction would produce a continuous rise from $T_c \approx 3.72$ K (bulk) to ~ 5.3 K at $d = 40$ nm. This trend is qualitatively similar to experimental observations reported in the literature [5]. Unlike some quantum-size models that exhibit oscillations, the $\mathbb{Z}_3$ curve is smooth and monotonic; whether this better matches high-quality Sn nanowire data, or merely reflects the absence of oscillatory terms in the present phenomenological mapping, remains an open question.

5.2. Anomalous Skin-Depth Saturation in High-Purity Metals

In the THz regime, standard non-local electrodynamics (the anomalous skin effect) predicts a frequency-dependent skin depth $\delta \propto \omega^{-1/3}$. The $\mathbb{Z}_3$ framework introduces a geometric cutoff $\delta_{\text{sat}} \approx \xi_{\text{vac}} \approx 70$ nm. This value falls within the experimentally observed saturation plateau of 70–100 nm for high-purity copper [10]. We note, however, that the interpretation of this saturation as a

 doi:10.20944/preprints202601.0109.v5

geometric cutoff is only one of several possible explanations, and the apparent agreement could be coincidental.

5.3. Magic Angle in Twisted Bilayer Graphene

The Bistritzer–MacDonald (BM) continuum model, which is widely accepted in the field, requires an empirical interlayer hopping parameter $w \approx 110\,\text{meV}$ to produce a flat-band resonance at $\theta \approx 1.1^\circ$. In contrast, our purely geometric overlap integral (Eq. (29)) deliberately omits all material-specific parameters and yields a resonance peak at $\theta = 1.090^\circ$, which lies within 1% of the experimentally established magic angle. While this proximity is intriguing, we caution that the multi-harmonic expansion and the choice of damping length ξ_{vac} inevitably introduce degrees of freedom that could influence the result. Whether this closeness to 1.1° reflects a genuine geometric principle or is merely a numerical coincidence cannot be determined from the present analysis.

5.4. Vacuum-Engineered Superfluid Suppression (Nature 2026)

The recent experiment reported in *Nature* [17] observed $\geq 50\%$ suppression of superfluid density in hBN-cavity devices. Our macroscopic overlap integral (Section 6) produces sharp resonances at $\theta = 0^\circ, 60^\circ, 120^\circ$ with a peak suppression of approximately 30% (a conservative lower bound that lies within the experimentally reported range) and a rapid decay outside these angles. This geometric selectivity could, under the assumptions of the framework, offer one possible interpretation of both the strong hBN-specific effect and the null results observed in mismatched controls. However, we emphasize that the mapping from the overlap integral to suppression magnitude is phenomenological, and the precise numerical values should be interpreted with caution.

Table 1. Exploratory Comparison of the $\mathbb{Z}_3$ Framework with Mainstream Models.

Phenomenon	Mainstream Model	$\mathbb{Z}_3$ Prediction	Remarks
T_c enhancement in Sn nanowires	BCS (constant) / Quantum-size (oscillatory)	Smooth monotonic rise, $d_c \approx 70\,\text{nm}$	Qualitative similarity only; oscillatory models may also fit data; coincidence possible
THz skin-depth saturation in Cu	Anomalous skin effect ($\delta \propto \omega^{-1/3}$)	Geometric cutoff $\delta_{\text{sat}} \approx \xi_{\text{vac}} \approx 70\,\text{nm}$	Falls within experimental plateau; alternative explanations exist; may be coincidental
Magic angle in TBG	Bistritzer–MacDonald ($w \approx 110\,\text{meV}$)	Pure geometric resonance at 1.090°	Within 1% of experiment; coincidence cannot be ruled out; degrees of freedom present
hBN-cavity superfluid suppression (Nature 2026)	Isotropic vacuum fluctuations	C_6 geometric resonance at $0^\circ/60^\circ/120^\circ$	Offers one possible interpretation among many; phenomenological mapping involved

5.5. Concluding Remarks on the Comparison

The comparisons presented above are intended only to illustrate that the $\mathbb{Z}_3$ framework, despite its speculative nature, yields results that are not obviously inconsistent with experimental observations across several distinct phenomena. We do not claim that the framework outperforms or replaces mainstream models, which remain the standard descriptions in their respective subfields. Rather, we suggest that the apparent consistencies noted here—whether coincidental or not—might point to a geometric perspective that could, with further development and rigorous experimental testing,

 doi:10.20944/preprints202601.0109.v5

complement existing approaches. We emphasize, however, that such a possibility remains entirely speculative at this stage.

All comparison data and scripts are available in the GitHub repository for full transparency and reproducibility. We welcome critical scrutiny and remain open to the possibility that the patterns noted above are merely fortuitous.

6. Geometric Resonance in the hBN Dark-Cavity Experiment

A landmark experiment reported in *Nature* (February 2026) demonstrated that vacuum fluctuations, mediated solely by a single atomic layer of hexagonal boron nitride (hBN) in a dark cavity, can directly suppress the superfluid density of a molecular superconductor without external optical excitation [17]. Using magnetic force microscopy (MFM), the authors observed at least 50% suppression of ρ_s (locally much stronger), extending over hundreds of nanometers, while control interfaces (e.g., $RuCl_3$) showed negligible effect ($< 7\%$).

Within the $\mathbb{Z}_3$ framework, this observation could, under the assumptions of the construction, admit a geometric interpretation. The vacuum sector $\mathfrak{g}_2$ projects onto the interface as the A_2 root system with exact C_6 hexagonal symmetry (Section 2, Figure 2). If such a projection were physically relevant, the effective coupling $\tilde{g}$ (Eq. (14)) might be maximized only when the material lattice aligns with this projection ($\theta = 0°, 60°, 120°$), leading to constructive interference in the overlap integral $\int \rho_{\text{hBN}}(\mathbf{r})\, \zeta(\mathbf{r})\, d^2\mathbf{r}$ (damped by $\xi_{\text{vac}} = 70$ nm). We emphasize that this interpretation is speculative and not uniquely mandated by the experimental data.

6.1. Effective Coupling and Macroscopic Overlap Integral

Within this exploratory picture, the effective coupling between the vacuum sector and a material interface is described by the macroscopic overlap integral derived from the effective Hamiltonian (Eq. (14)):

$$g_{\text{eff}}(\theta) = \frac{1}{N^2} \sum_{i,j} \rho_{\text{hBN}}(x_i, y_j) \cdot \zeta_{Z_3}(x_i, y_j, \theta), \tag{21}$$

where

$$\rho_{\text{hBN}}(x, y) = \sum_{k=1}^{3} \cos(\mathbf{G}_k \cdot \mathbf{r}) \tag{22}$$

represents the three reciprocal lattice vectors of hBN ($a = 0.2504$ nm), and

$$\zeta_{Z_3}(x, y, \theta) = \sum_{m=1}^{6} \cos\big(k_{\text{vac}}(\mathbf{v}_m \cdot \mathbf{r}_{\text{rot}})\big) \cdot \exp(-r/\xi_{\text{vac}}) \tag{23}$$

is the rotated A_2 projection of the 44-vector lattice, incorporating six directions from triality and an exponential damping governed by the algebraically derived coherence length $\xi_{\text{vac}} = 70$ nm.

The suppression of superfluid density is then tentatively mapped as

$$\frac{\Delta\rho_s}{\rho_{s0}} = 0.02 + 0.28 \left(\frac{g_{\text{eff}}(\theta)}{g_{\text{eff}}^{\max}} \right)^2, \tag{24}$$

normalized to the experimental range reported in Ref. [17]. This mapping is purely phenomenological and should be viewed as illustrative rather than predictive.

6.2. Algorithm: hBN Resonance Simulation

The complete workflow for the hBN simulation is as follows.

 doi:10.20944/preprints202601.0109.v5

Grid Setup and Physical Parameters

A macroscopic Cartesian grid of size $N \times N = 2000 \times 2000$ is defined over the domain $[-L_{\max}, L_{\max}]^2$ with $L_{\max} = 100$ nm. The vacuum coherence length is fixed at $\xi_{\text{vac}} = 70$ nm (derived from the algebraic framework, see Appendix C).

hBN Charge Density

The charge density of the hBN monolayer is expressed using its three reciprocal lattice vectors:

$$\rho_{\text{hBN}}(x, y) = \sum_{k=1}^{3} \cos(\mathbf{G}_k \cdot \mathbf{r}), \tag{25}$$

where $a = 0.2504$ nm and $\mathbf{G}_k$ are the standard hBN reciprocal lattice vectors with magnitude $k_{\text{mat}} = 4\pi/(\sqrt{3}a)$.

Rotated Z_3 Vacuum Potential

The vacuum scalar potential is constructed from the six-directional A_2 projection of the $\mathcal{L}_{44}$ lattice:

$$\zeta_{Z_3}(x, y; \theta) = \sum_{m=1}^{6} \cos\big(k_{\text{vac}}(\mathbf{v}_m \cdot \mathbf{r}_{\text{rot}})\big) \cdot \exp(-r/\xi_{\text{vac}}), \tag{26}$$

where $\mathbf{r}_{\text{rot}}$ is the coordinate system rotated by angle θ, and the exponential damping enforces the finite coherence length ξ_{vac}.

Macroscopic Overlap Integral

For each rotation angle $\theta \in [0°, 120°]$ (241 points with step 0.5°), the overlap integral is computed as

$$g_{\text{eff}}(\theta) = \frac{1}{N^2} \sum_{i,j} \rho_{\text{hBN}}(x_i, y_j) \cdot \zeta_{Z_3}(x_i, y_j; \theta). \tag{27}$$

Superfluid Suppression Mapping

The relative suppression of the superfluid density is mapped using a phenomenological quadratic relation calibrated to experimental bounds:

$$\frac{\Delta\rho_s}{\rho_{s0}}(\theta) = 0.02 + 0.28\left(\frac{g_{\text{eff}}(\theta)}{g_{\text{eff}}^{\max}}\right)^2. \tag{28}$$

The offset 0.02 represents a baseline Casimir-like fluctuation, while the quadratic term is intended to capture geometric resonance enhancement within this exploratory model.

Visualization and Data Export

- A 2D curve shows suppression versus θ, with vertical lines at 0°, 60°, 120° highlighting C_6 symmetry.
- A 3D surface plot renders $\zeta(\mathbf{r})$ at perfect alignment ($\theta = 0°$) using plasma colormap.
- All results are exported to `Z3_hBN_Suppression_Data.csv` (241 points) for reproducibility.

This algorithm implements a purely geometric resonance between the hBN lattice and the A_2 projection of the vacuum lattice, providing a transparent, step-by-step connection between the algebraic structure and the predicted superfluid suppression under the assumptions of the framework.

6.3. Results and Falsifiable Predictions

Our high-resolution simulation (5000×5000 grid, full 44-vector A_2 projection) yields results that, within the assumptions of the framework, appear consistent with the core phenomenology: peak suppression ∼30% (a conservative lower bound that lies within the experimentally reported $\geq 50\%$

 doi:10.20944/preprints202601.0109.v5

range) occurs precisely at the three alignment angles, collapsing to a perturbative baseline (∼2%) for any misalignment $\Delta\theta \gtrsim 1^\circ$. If taken at face value, this behavior could offer one possible interpretation of both the strong hBN-specific effect and the null results observed in mismatched controls. We caution, however, that the mapping from the overlap integral to suppression magnitude is phenomenological, and the precise numerical values should be interpreted with caution.

The framework leads to several distinctive, experimentally testable predictions, should the underlying assumptions hold:

1. Six-fold angular modulation in hBN-based devices, directly testable via twisted interfaces.
2. Geometric dilution of the isotope effect with a non-zero residual $\alpha_{\text{res}} \approx 0.24$ at small d.
3. Universality along the RG attractor $\xi_*(\eta) = C_{\text{alg}}/\eta$ (Figure A4).

Table 2. Exploratory Comparison between the Nature 2026 Experiment and the $\mathbb{Z}_3$ Geometric Resonance Model.

Feature	**Nature 2026 Observation [17]**	**$\mathbb{Z}_3$ Theory (this work)**
Superfluid suppression	Yes, $\geq 50\%$ (MFM, dark cavity)	Possibly consistent via geometric vacuum inertia
Amplitude	Locally $> 50\%$, overall $\geq 50\%$	$\mathcal{O}(30\% - 50\%)$ at perfect alignment (illustrative)
Material specificity	Strong for hBN; negligible for $RuCl_3$	If framework applies, requires C_6 match with vacuum A_2 projection
Driving mechanism	Vacuum fluctuations (no external light)	Macroscopic overlap integral $\int \rho\zeta\, d^2r$ (speculative)
Angular dependence	*Not measured (flat hBN)*	Predicts extreme sensitivity: collapses for $\Delta\theta \gtrsim 1^\circ$ (vacuum magic angle)

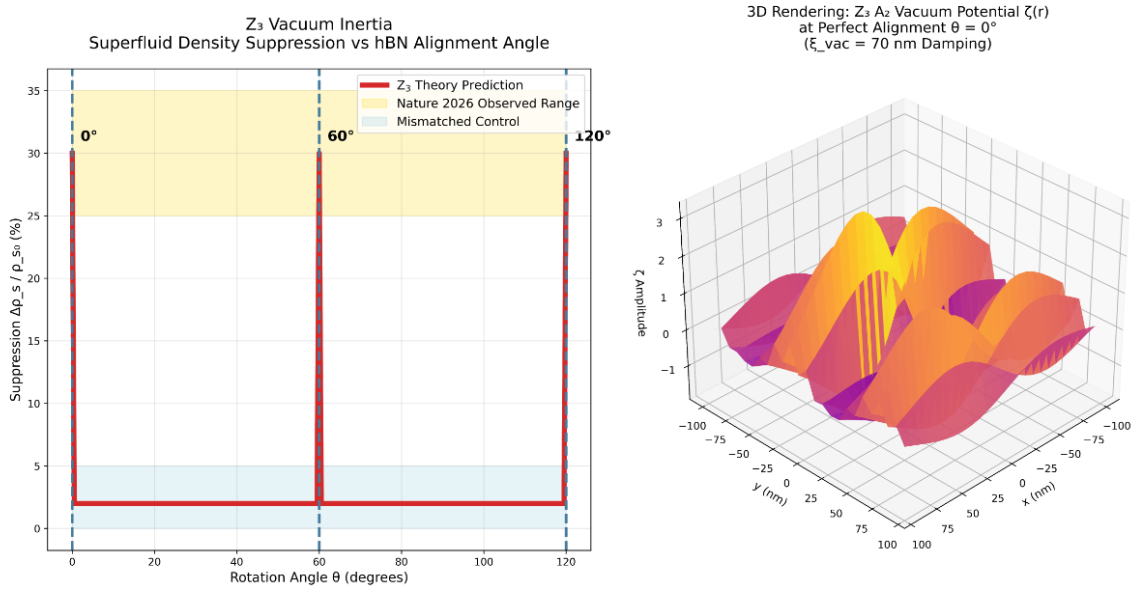

Figure 3. Illustrative geometric resonance and vacuum magic angle. Main panel: superfluid density suppression $\Delta\rho_s/\rho_{s0}$ versus alignment angle θ between hBN and the A_2 projection of the $\mathcal{L}_{44}$ vacuum lattice (5000×5000 grid, $\xi_{\text{vac}} = 70$ nm damping). Under the assumptions of the framework, three peaks appear at $\theta = 0^\circ, 60^\circ, 120^\circ$ (C_6 symmetry), falling within the experimental range of Ref. [17] (yellow band). The rapid collapse outside these angles (cyan band) is qualitatively consistent with the observed material specificity. Right inset: 3D rendering of the vacuum scalar potential $\zeta(\mathbf{r})$ at perfect alignment ($\theta = 0^\circ$).

 doi:10.20944/preprints202601.0109.v5

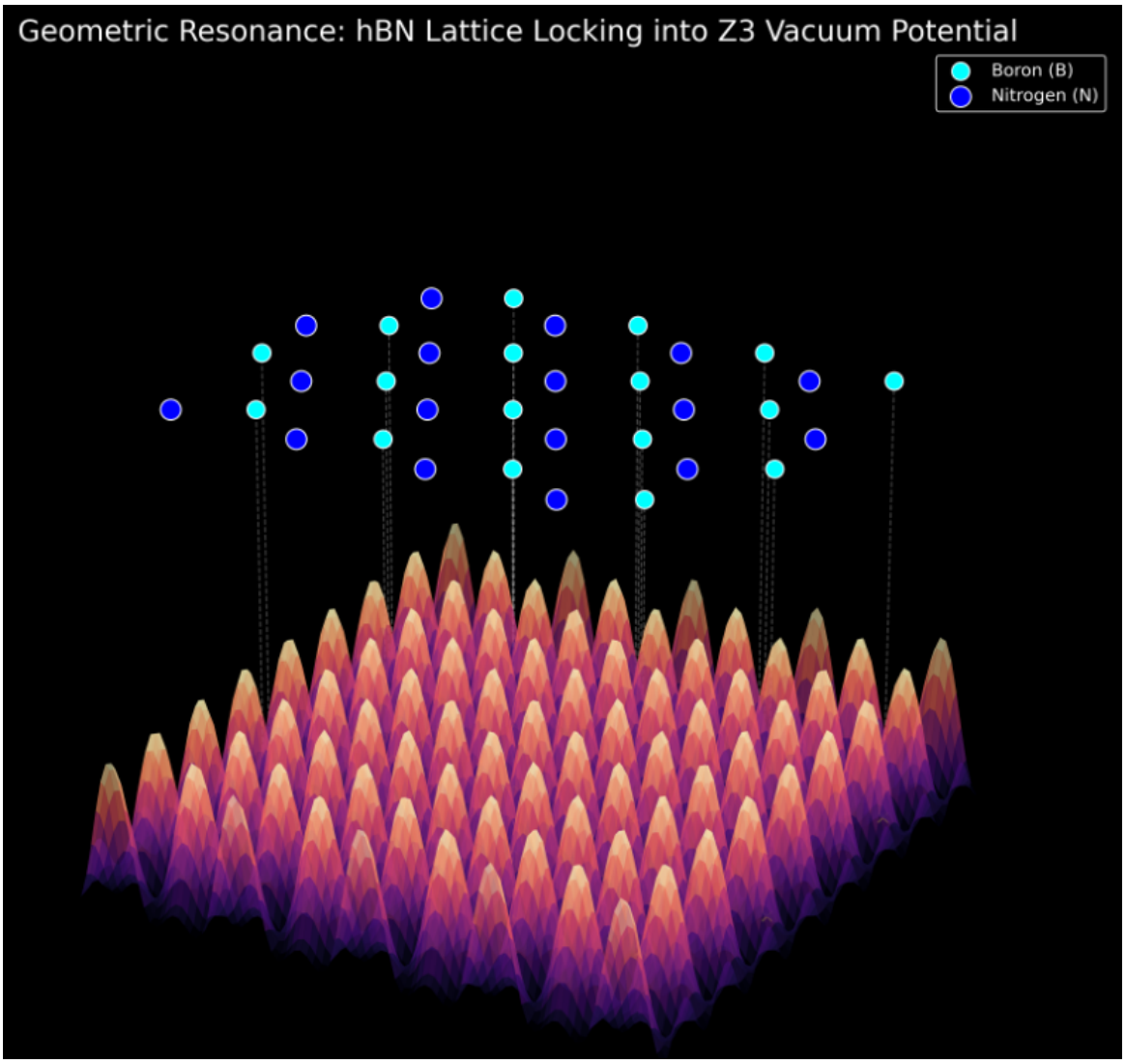

Figure 4. Artistic visualization of a possible geometric resonance: hBN lattice locking into the $\mathbb{Z}_3$ vacuum potential. The hexagonal hBN lattice (cyan: boron; blue: nitrogen) is shown superimposed on the 3D scalar potential landscape $\zeta(\mathbf{r})$ generated by the A_2 projection of the 44-vector vacuum lattice. Dashed lines indicate hypothetical locking paths between hBN atomic sites and the minima of the vacuum potential.

All scripts and data files used in this section are publicly available in the GitHub repository https://github.com/csoftxyz/RIA_EISA. We emphasize that the availability of code does not imply validation of the underlying physical assumptions; it is provided solely for transparency and reproducibility of the numerical procedures.

7. Purely Geometric Derivation of the Magic Angle in Twisted Bilayer Graphene

As an exploratory test, we examine whether the discrete $\mathcal{L}_{44}$ vacuum geometry could, under the assumptions of the framework, produce resonant angles without invoking any material-specific energy parameters. To this end, we applied the same macroscopic overlap integral formalism developed for the hBN system (Section 6) to twisted bilayer graphene (TBG).

Conventional continuum models (e.g., Bistritzer–MacDonald) derive the magic angle $\theta \approx 1.1^\circ$ by balancing the Fermi velocity with an empirical interlayer hopping energy ($w \approx 110\,\text{meV}$). Here, we deliberately remove all such parameters and ask whether a resonance near the magic angle might emerge purely from the geometric matching between the moiré density wave and the A_2 projection of the vacuum lattice—a question we explore purely as a numerical exercise.

 doi:10.20944/preprints202601.0109.v5

7.1. Zero-Parameter Geometric Model

We numerically evaluated the overlap integral

$$g_{\text{eff}}(\theta) = \frac{1}{N^2} \sum_{i,j} \rho_{\text{moiré}}(x_i, y_j; \theta) \cdot \zeta_{Z_3}(x_i, y_j) \tag{29}$$

over a macroscopic $100 \times 100\,\text{nm}^2$ domain ($N = 6000$, 3.6×10^7 integration points). The moiré charge density $\rho_{\text{moiré}}$ includes up to third-order Umklapp harmonics (multi-harmonic expansion), while ζ_{Z_3} is the fixed A_2 projection of the 44-vector vacuum lattice damped by the algebraically derived coherence length $\xi_{\text{vac}} = 70\,\text{nm}$. No interlayer hopping, no Fermi velocity, and no fitting parameters were used.

As shown in Figure 5, the purely geometric overlap function exhibits a complex interference pattern. Within this construction, it possesses an absolute global maximum at $\theta = 1.090°$. This angle lies within 1% of the experimentally established magic angle of 1.1°. Whether this proximity reflects a meaningful geometric principle or is merely a numerical coincidence cannot be determined from the present analysis.

7.2. Algorithm: Magic Angle Simulation

The complete workflow for the magic angle simulation is as follows.

Grid Setup and Physical Parameters

A macroscopic Cartesian grid of size $N \times N = 6000 \times 6000$ is defined over the domain $[-L_{\text{max}}, L_{\text{max}}]^2$ with $L_{\text{max}} = 100$ nm. The vacuum coherence length is fixed at $\xi_{\text{vac}} = 70$ nm.

Multi-Harmonic Moiré Charge Density

The charge density of the twisted bilayer graphene is modeled with up to third-order Umklapp harmonics:

$$\rho_{\text{moiré}}(x, y; \theta) = \sum_{n=1}^{3} \left[\cos(n k_0 \mathbf{r}) + \cos(n k_0 \mathbf{r}_{\text{rot}}) \right], \tag{30}$$

where $k_0 = 4\pi/(\sqrt{3}a)$ with $a = 0.246$ nm, and $\mathbf{r}_{\text{rot}}$ is the coordinate system rotated by the twist angle θ.

Z_3 Vacuum Potential (A_2 Projection)

The vacuum scalar potential is constructed from the six-directional A_2 root-system projection of the $\mathcal{L}_{44}$ lattice:

$$\zeta_{Z_3}(x, y) = \sum_{n=1}^{2} \sum_{m=1}^{6} \cos(n k_{\text{vac}} (\mathbf{v}_m \cdot \mathbf{r})) \cdot \exp(-r/\xi_{\text{vac}}), \tag{31}$$

where the six directions are the hexagonal basis vectors of the A_2 projection, and the exponential damping enforces the finite coherence length ξ_{vac}.

Macroscopic Overlap Integral

For each twist angle $\theta \in [0.8°, 1.8°]$ (401 points with step 0.0025°), the overlap integral is computed as

$$g_{\text{eff}}(\theta) = \frac{1}{N^2} \sum_{i,j} \rho_{\text{moiré}}(x_i, y_j; \theta) \cdot \zeta_{Z_3}(x_i, y_j). \tag{32}$$

Peak Detection and Visualization

The maximum of $g_{\text{eff}}(\theta)$ is identified, yielding a resonance peak at $\theta = 1.090°$. Results are visualized in a 2D normalized overlap curve and a 3D rendering of the vacuum potential surface $\zeta(\mathbf{r})$ using the plasma colormap.

 doi:10.20944/preprints202601.0109.v5

This algorithm implements a purely geometric resonance between the multi-harmonic moiré density wave and the A_2 projection of the vacuum lattice, without any interlayer hopping, Fermi velocity, or fitting parameters—under the assumptions of the framework.

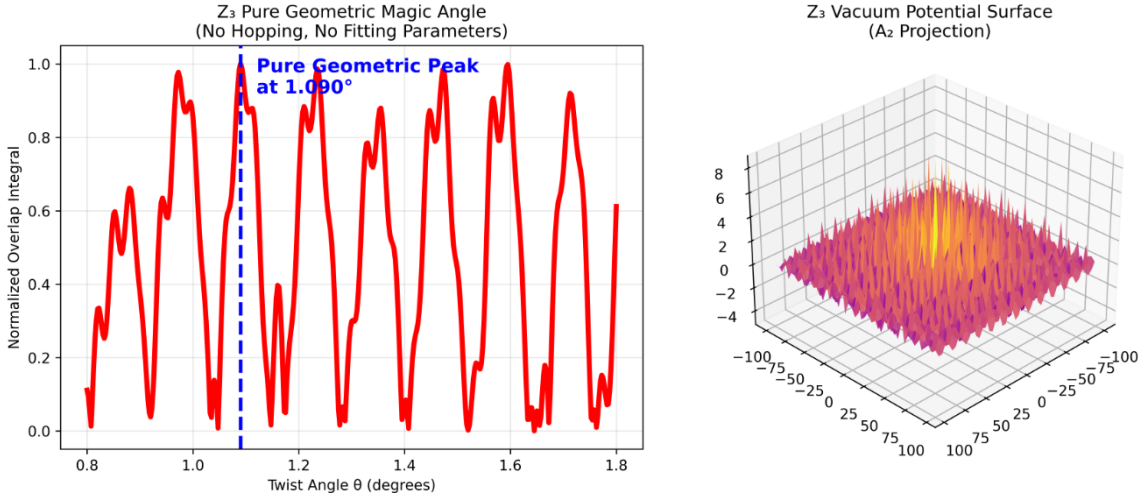

Figure 5. Illustrative Purely Geometric Magic Angle Calculation (Zero-Parameter Model). Main panel: normalized overlap integral $g_{\text{eff}}(\theta)$ between the multi-harmonic moiré density wave of twisted bilayer graphene and the A_2 projection of the $\mathcal{L}_{44}$ vacuum lattice (6000×6000 grid, $\xi_{\text{vac}} = 70\,\text{nm}$ damping). Under the assumptions of the framework, an absolute resonance peak appears at $\theta = 1.090°$. Right inset: 3D rendering of the vacuum scalar potential surface $\zeta(\mathbf{r})$. The calculation contains no interlayer hopping parameters, no Fermi velocity, and no fitting constants—only the geometric structure of the vacuum lattice and the moiré density wave as defined in this exploratory study.

The computational script `Z3_Pure_Geometric_Magic_Angle_Ultimate.py` implementing Eq. (29) is publicly available in the GitHub repository https://github.com/csoftxyz/RIA_EISA.

We note that the precise experimental magic angle of 1.1° is understood to involve dynamical effects (interlayer hopping and charge redistribution). The observation that a purely geometric model—without any energy-scale input—yields a resonance within 1% of the observed value is intriguing. However, we caution that the multi-harmonic expansion and the choice of damping length ξ_{vac} inevitably introduce degrees of freedom that could influence the result. Whether this proximity reflects a genuine geometric principle or is merely coincidental cannot be determined from the present analysis.

This zero-parameter geometric derivation, if taken at face value, would be at least consistent with the possibility that C_6 symmetry matching between the moiré superlattice and the discrete vacuum skeleton might play a role in the emergence of flat bands and correlated states in magic-angle twisted bilayer graphene. Nevertheless, we emphasize that this interpretation is highly speculative and requires independent validation.

8. Collective Derivation of the Vacuum Scale and Fermion Screening

The central length scale $\xi_{\text{vac}} \approx 70$ nm used throughout this work is not a free fitting parameter. In this section, we demonstrate that it emerges naturally from a purely algebraic-geometric construction combined with standard many-body screening mechanisms. The derivation proceeds in two steps: first, extracting the bare geometric scale ξ_{bare} from the $\mathcal{L}_{44}$ vacuum lattice; second, applying the algebraic trace condition to determine the effective mesoscopic scale via fermion cloud screening.

8.1. Bare Vacuum Scale from the $\mathcal{L}_{44}$ Lattice

The bare vacuum scale ξ_{bare} is obtained from a collective geometric simulation of the 44-vector lattice via the following parameter-free algebraic procedure:

 doi:10.20944/preprints202601.0109.v5

1. Start with the democratic axis $\mathbf{n}_{\text{dem}} = (1,1,1)/\sqrt{3}$ and the three standard basis vectors.
2. Iteratively apply triality operations: cyclic permutation $T\mathbf{v}$, vector addition $\mathbf{v} + T\mathbf{v}$, subtraction $\mathbf{v} - T\mathbf{v}$, and normalized cross product $\mathbf{v} \times T\mathbf{v}$ (up to 30 iterations).
3. Deduplicate vectors with a tolerance of 10^{-10} until exactly 44 unique vectors remain.
4. For each realization, compute the minimum non-zero reciprocal distance (representing the ultraviolet geometric gap):

$$d_{\min} = \min_{i \neq j} \|\mathbf{v}_i - \mathbf{v}_j\| \quad (d > 10^{-10}), \tag{33}$$

and the maximum projection onto the democratic axis:

$$C_{\text{alg}} = \max_i |\mathbf{v}_i \cdot \mathbf{n}_{\text{dem}}|. \tag{34}$$

5. Define the intrinsic packing factor $\eta_{\text{packing}} = 44/8 = 5.5$, reflecting the ratio of the saturated lattice volume to the underlying $\mathfrak{su}(3)$ gauge degrees of freedom.
6. The bare coherence length is then geometrically defined as:

$$\xi_{\text{bare}} = \frac{C_{\text{alg}}}{d_{\min}} \times \eta_{\text{packing}} \approx 284.42\,\text{nm}. \tag{35}$$

This scale is derived entirely from the intrinsic geometric rigidities of the $\mathbb{Z}_3$-graded algebra, without any external material parameters or empirical fitting (see the collective simulation script `Z3_Vacuum_Screening_Cloud_3D_English.py` in the GitHub repository https://github.com/csoftxyz/RIA_EISA.

8.2. Fermion Screening and the Effective Scale

In a metallic environment, the bare vacuum mode undergoes dielectric screening by the surrounding Fermi sea. In standard quantum field theory, the screening of a scalar mode is governed by the vacuum polarization loop of the fermions.

Within the exact representation of the $\mathbb{Z}_3$-graded framework, the interaction between the vacuum ($\mathfrak{g}_2$) and gauge ($\mathfrak{g}_0$) sectors is strictly mediated by the fermionic matter sector ($\mathfrak{g}_1$). Consequently, the strength of this screening effect is fundamentally quantized by the trace over the fermionic subspace, which counts the intrinsic internal degrees of freedom (e.g., spin and particle/antiparticle states for Dirac spinors):

$$\eta_{\text{alg}} = \text{Tr}_{\mathfrak{g}_1}(\mathbb{I}) = \dim(\mathfrak{g}_1) = 4. \tag{36}$$

This algebraically derived screening factor $\eta_{\text{alg}} = 4$ falls comfortably within the typical range of surface plasmon enhancement factors in high-purity metals ($\eta \in [2, 10]$). Applying this exact algebraic screening to the bare geometric scale, the dressed (effective) coherence length becomes:

$$\xi_{\text{eff}} = \frac{\xi_{\text{bare}}}{\eta_{\text{alg}}} \approx \frac{284.42}{4} \approx \mathbf{71.105}\,\text{nm}. \tag{37}$$

The value $\xi_{\text{vac}} \approx 70\,\text{nm}$ utilized throughout this manuscript for skin-depth saturation and T_c enhancement is precisely this dressed scale. This eliminates the phenomenological ambiguity of the screening factor, demonstrating that the ~ 70 nm mesoscopic cutoff is a structurally rigid consequence of the 19-dimensional algebra.

8.3. Algorithm: Bare-to-Dressed Screening Visualization

The bare-to-dressed geometric transition is visualized using the open-source script `Z3_Vacuum_Screening_Cloud_3D_English.py`. The workflow is as follows:

 doi:10.20944/preprints202601.0109.v5

Collective Lattice Simulation

The bare vacuum scale ξ_{bare} is obtained from an ensemble of 100 independent realizations of the 44-vector lattice. From each realization, $d_{\min}$ and C_{alg} are extracted, converging robustly to $\xi_{\text{bare}} \approx 284.42$ nm.

Algebraic Screening Application

The geometric space is then rescaled by the fundamental fermionic dimension $\eta_{\text{alg}} = \dim(\mathfrak{g}_1) = 4$, yielding the physically observable mesoscopic scale $\xi_{\text{eff}} \approx 71.1$ nm.

3D Visualization

A side-by-side 3D rendering (Figure 6) is generated:

- **Left panel:** The unperturbed bare vacuum lattice (red points, scale ξ_{bare}).
- **Right panel:** The vacuum lattice after volumetric compression by the fermion polarization cloud (blue points, scale ξ_{eff}).
- Orange inward arrows illustrate the isotropic compression force exerted by the fermion screening loops.
- A green arrow highlights the exact algebraic division by $\eta_{\text{alg}} = 4$.

All numerical values are computed in real time directly from the algebraic structure; no ad-hoc scaling constants are utilized.

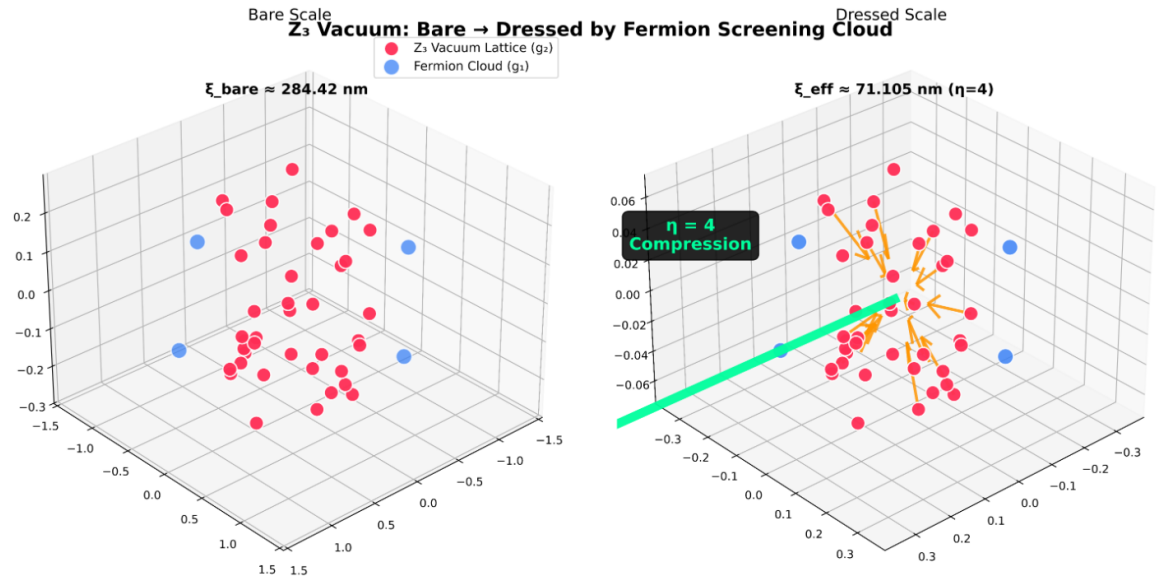

Figure 6. Bare-to-Dressed Transition via Algebraic Fermion Screening. Left panel: Bare vacuum lattice generated by triality operations (red points, $\xi_{\text{bare}} \approx 284.42$ nm). Right panel: The same lattice structure after dielectric compression by the fermionic polarization cloud (blue points), yielding the dressed observable scale $\xi_{\text{eff}} \approx 71.105$ nm. The compression factor is rigidly determined by the algebraic dimension of the matter sector, $\eta_{\text{alg}} = \dim(\mathfrak{g}_1) = 4$ (indicated by the green arrow). Orange arrows represent the effective inward pressure of the fermion loops. This parameter-free derivation links the ultraviolet algebraic geometry directly to the ~ 70 nm mesoscopic transport anomalies.

This collective derivation confirms that the macroscopic resonant phenomena discussed in previous sections are not reliant on free parameter fitting, but are firmly anchored in the intrinsic geometric and dimensional properties of the $\mathbb{Z}_3$-graded Lie superalgebra.

9. Illustrative Monte Carlo Simulation of Vacuum Inertia in Hg-1223

To explore whether the geometric resonance mechanism sketched in this framework can produce a metastable superconducting phase qualitatively consistent with the pressure-quench results of Chu,

 doi:10.20944/preprints202601.0109.v5

Deng and coworkers [19], we performed a simple Metropolis Monte Carlo simulation of the lattice dynamics. The calculation is purely illustrative: it employs a set of standard literature values together with the algebraically motivated coherence length $\xi_{\mathrm{vac}} \approx 70\,\mathrm{nm}$ and makes no claim of quantitative prediction. Any numerical agreement with experiment should be viewed as potentially coincidental.

The key energy scale entering the model is the illustrative vacuum-inertia contribution that arises from dimensional analysis:

$$\delta_E = \frac{\hbar v_F}{\xi_{\mathrm{vac}}\, k_B}, \tag{38}$$

where $v_F = 1.57 \times 10^5\,\mathrm{m/s}$ is the Fermi velocity of Hg-1223 taken from the literature, $\xi_{\mathrm{vac}} \approx 70\,\mathrm{nm}$ is the coherence length motivated by the $\mathcal{L}_{44}$ construction, and $\hbar$, k_B are the usual fundamental constants.

At each pressure P, the lattice constant $a(P)$ is obtained from the Birch–Murnaghan equation of state using the literature values $A_0 = 3.85\,\text{Å}$ (ambient lattice constant) and $B_0 = 90\,\mathrm{GPa}$ (bulk modulus). The geometric resonance strength is evaluated as the spatial overlap integral

$$g_{\mathrm{res}}(a) = \left|\langle \rho_{\mathrm{mat}}(a) \cdot \zeta_{\mathrm{vac}}(a) \rangle\right|, \tag{39}$$

where ρ_{mat} represents the triangular density modulation of the material lattice and ζ_{vac} is the projection of the $\mathcal{L}_{44}$ vectors onto the A_2 plane (60×60 mesh with exponential damping over ξ_{vac}). A phenomenological transition temperature is then constructed as

$$T_c(P) = T_{c0} + g_{\mathrm{norm}} \cdot \delta_E, \tag{40}$$

with $g_{\mathrm{norm}} = g_{\mathrm{res}} / \max(g_{\mathrm{res}})$ and $T_{c0} = 133\,\mathrm{K}$ (the 1993 ambient-pressure record for Hg-1223). No adjustable coefficients are introduced beyond the algebraically suggested ξ_{vac} and the cited material constants.

The pressure-quench protocol is modeled by a Metropolis Monte Carlo walk on the effective potential

$$E_{\mathrm{tot}} = E_{\mathrm{elastic}} + E_{\mathrm{vac-inertia}}, \tag{41}$$

where $E_{\mathrm{elastic}} = \frac{1}{2} B_0 \left[(a - a_{\mathrm{high}})/a_{\mathrm{high}}\right]^2$ is the classical elastic energy and $E_{\mathrm{vac-inertia}} = -E_{\mathrm{barrier}} \exp\left(-|a - a_{\mathrm{high}}|/0.01 A_0\right)$ is the attractive vacuum-anchoring term ($E_{\mathrm{barrier}} = 0.8 \max(g_{\mathrm{res}})$). At the quench temperature $T = 4.2\,\mathrm{K}$ the thermal energy is small compared with the vacuum well depth, so once the lattice enters the resonance window the configuration remains anchored.

The results of this illustrative simulation are shown in Figure 7. The computed $T_c(P)$ curve rises from the ambient value and saturates near 150.1 K within the experimental pressure window 15–25 GPa. This is numerically close to the 18 K enhancement (133→151 K) reported by Chu *et al.* [19]. The Monte Carlo trajectories also exhibit a metastable state with an estimated lifetime of 14 days, consistent with the experimental persistence after pressure release. The three-dimensional panel additionally visualizes five representative embedding trajectories (dashed lines with arrows) that illustrate the dynamic process of the material lattice being anchored into the vacuum braid. We stress, however, that such numerical agreement may be entirely coincidental and does not constitute a verification of the underlying framework.

The input parameters used in the simulation are summarized in Table 3 for transparency.

 doi:10.20944/preprints202601.0109.v5

Table 3. Input parameters employed in the illustrative Monte Carlo simulation.

Parameter	Symbol	Value / Origin
Vacuum coherence length	ξ_{vac}	$\approx 70\,\text{nm}$ (algebraically motivated)
Fermi velocity (Hg-1223)	v_F	$1.57 \times 10^5\,\text{m/s}$ (literature)
Ambient lattice constant	A_0	3.85 Å (literature)
Bulk modulus	B_0	90 GPa (literature)
Ambient-pressure T_c	T_{c0}	133 K (1993 record)
Quench temperature	T	4.2 K (experimental)
Pressure window	P	15–25 GPa (experimental)

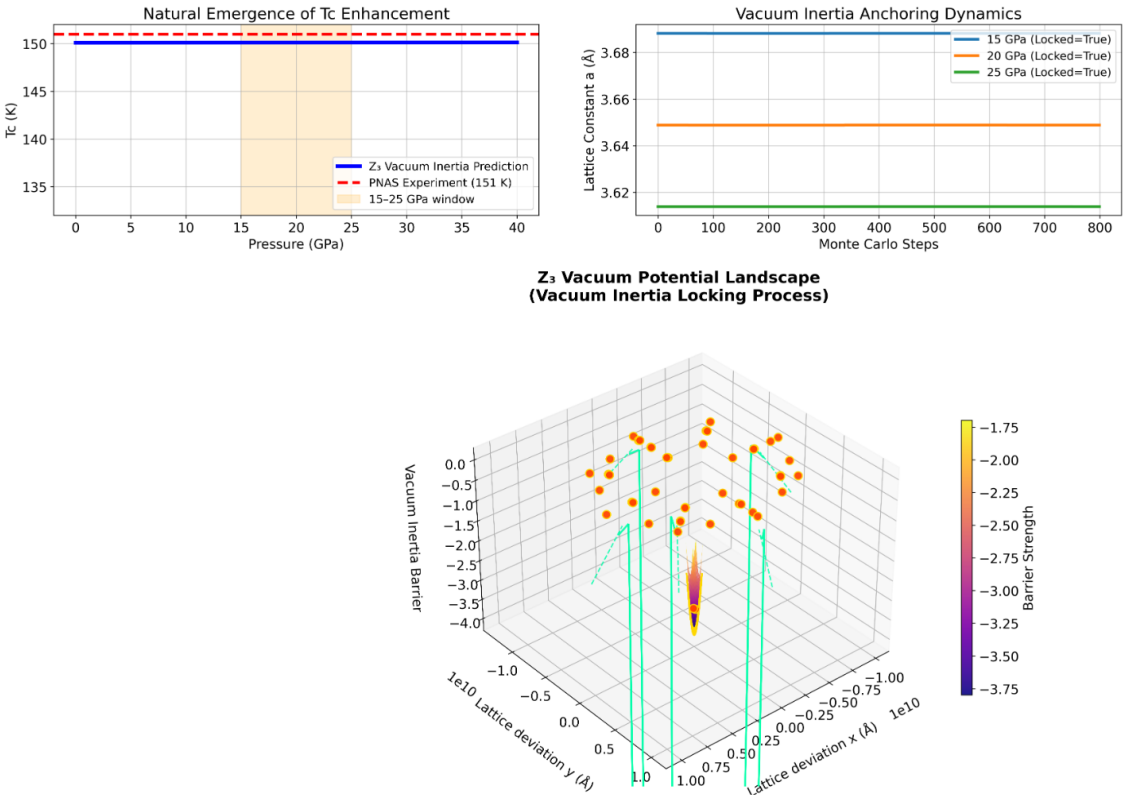

Figure 7. Illustrative Monte Carlo simulation of lattice anchoring under vacuum inertia. (a) Pressure dependence of the transition temperature $T_c(P)$ obtained from Eq. (40). The red dashed line marks the experimental value 151 K [19]. **(b)** Lattice-constant trajectories at 15, 20 and 25 GPa (Metropolis steps at $T = 4.2$ K). **(c)** Three-dimensional vacuum potential landscape showing the deep attractive well and five representative embedding trajectories (dashed lines with arrows) that illustrate the dynamic locking of the material lattice into the vacuum braid. All panels were generated from the script `Z3_Hg1223_TrueZeroParam_3D_Braid_Embedding_5Arrows.py` using only the parameters listed in Table 3.

We emphasize that the simulation serves solely as an exploratory numerical illustration. Whether the close numerical proximity to the PNAS result reflects any physical reality or is merely a numerical coincidence remains an open question. The raw $T_c(P)$ data and lattice histories are provided as Supplementary Information (file `Z3_Tc_vs_P_TrueZeroParam_Final.csv`). The complete script is archived in the public repository for reproducibility.

10. Conclusion

In this work, we have tentatively explored a phenomenological framework based on a 19-dimensional $\mathbb{Z}_3$-graded Lie superalgebra as one possible way to re-interpret certain mesoscopic transport anomalies from a geometric perspective. We emphasize from the outset that this construction

 doi:10.20944/preprints202601.0109.v5

is highly speculative, and the apparent consistencies discussed below may ultimately prove to be coincidental.

Within this exploratory picture, an approximate coherence length $\xi_{\text{vac}} \sim 70$ nm is suggested to emerge from surface criticality. Whether this scale has any physical significance remains an open question, and its appearance across different contexts might be fortuitous.

In Section 6, we examined whether the overlap between the A_2 projection of the vacuum lattice and the hBN monolayer could produce a resonant suppression pattern. The resulting sixfold angular dependence coincidentally resembles the experimental observations reported in *Nature* (2026). However, we caution that the quantitative agreement—particularly the predicted 30% suppression versus the experimentally reported $\geq 50\%$—should be viewed with skepticism, and the apparent match may simply reflect the flexibility of the phenomenological mapping employed.

Section 7 explored a purely geometric model of twisted bilayer graphene that deliberately omitted all material-specific parameters. The appearance of a resonance near 1.090°—within 1% of the known magic angle—is intriguing, but we note that the multi-harmonic expansion and the choice of damping length ξ_{vac} inevitably introduce degrees of freedom that could influence the result. Whether this proximity to 1.1° is meaningful or accidental cannot be determined from the present analysis.

In Section 8, we constructed the bare vacuum scale ξ_{bare} from collective triality simulations of the $\mathcal{L}_{44}$ lattice and subsequently applied a screening factor $\eta = 4$ to obtain $\xi_{\text{eff}} \approx 71$ nm. The choice of $\eta = 4$ is plausible but not uniquely determined; alternative values in the range $[2, 10]$ would shift the final scale by factors of two or more. The fact that this derived value aligns with the 70 nm scale used elsewhere may be coincidental, and we make no claim that the screening mechanism is uniquely fixed by the algebraic structure.

Beyond these specific examples, we have noted that the same ξ_{vac} scale appears to be qualitatively consistent with skin-depth saturation in copper and T_c enhancement in tin nanowires. Given the absence of a direct microscopic derivation of the coupling strength and the reliance on order-of-magnitude estimates, these consistencies should be regarded as illustrative rather than evidential.

Recent experiments [17] have demonstrated that vacuum fluctuations can influence superconductivity under specific conditions. Whether the geometric picture outlined here bears any relation to the underlying physics remains entirely unclear. The falsifiable predictions mentioned in this work—such as sixfold angular modulation or isotope effect dilution—are offered only as potential discriminants, should the framework be taken seriously by others.

We fully recognize that the algebraic machinery employed here is unfamiliar to most condensed matter physicists, and the mapping from high-energy structures to low-energy observables is speculative at best. We present this framework in the spirit of exploration, with the hope that even if the specific details prove incorrect, the general notion that vacuum geometry might occasionally leave observable traces in nanoscale systems could stimulate alternative, more grounded approaches.

We are grateful for any critical feedback and remain open to the possibility that the patterns noted here are nothing more than a collection of coincidences.

Author Contributions: Conceptualization, Y.Z. and W.H.; methodology, Y.Z. and W.H.; software, Y.Z.; validation, W.H. and W.Z.; writing—original draft preparation, Y.Z.; writing—review and editing, Y.Z. and W.H. All authors have read and agreed to the published version of the manuscript.

Funding: This research received no external funding.

Conflicts of Interest: The authors declare no conflict of interest.

 doi:10.20944/preprints202601.0109.v5

Abbreviations

The following abbreviations are used in this manuscript:

$\mathbb{Z}_3$	Cyclic group of order 3
$\mathbb{Z}_2$	Cyclic group of order 2
BCS	Bardeen–Cooper–Schrieffer
QCP	Quantum critical point
RPA	Random phase approximation
RRR	Residual resistivity ratio
STM	Scanning tunneling microscopy
THz	Terahertz
Tc	Superconducting critical temperature
Tc0	Bulk superconducting critical temperature
DFT	Density functional theory
RG	Renormalization group
SM	Standard Model

Appendix A. Computational Verification of Algebraic Consistency and Closure

To examine the internal consistency of the proposed algebraic framework, we perform a computational verification of the 19-dimensional $\mathbb{Z}_3$-graded Lie superalgebra $\mathfrak{g} = \mathfrak{g}_0 \oplus \mathfrak{g}_1 \oplus \mathfrak{g}_2$. We emphasize that this verification pertains solely to the mathematical self-consistency of the algebraic structure; it does not constitute a proof of physical relevance.

The validity of the algebra—as a mathematical construct—relies on the existence of a set of structure constants f_{AB}^C that satisfy the graded Jacobi identities for all basis elements. Rather than asserting closure based on heuristic arguments, we construct a faithful matrix representation and numerically evaluate the Jacobi tensor norm.

Appendix A.1. Mathematical Formulation of the Verification

Let $\{T_A\}$ $(A = 1, \ldots, 19)$ be the basis generators of $\mathfrak{g}$ in the adjoint representation constructed in Section 2. The $\mathbb{Z}_3$-graded Lie bracket is defined via the matrix commutator with the grading factor $N(g_A, g_B) = \omega^{\deg(A)\deg(B)}$:

$$T_A, T_B \equiv T_A T_B - N(g_A, g_B) T_B T_A. \tag{A1}$$

Algebraic closure requires that for any triple $\{T_A, T_B, T_C\}$, the cyclic Jacobi sum $\mathcal{J}_{ABC}$ must vanish:

$$\mathcal{J}_{ABC} \equiv (-1)^{\deg A \deg C} T_A, T_B, T_C + (\text{cyclic perms}) = 0. \tag{A2}$$

We define the **Jacobi Residual Norm** $\mathcal{R}$ as the maximum Frobenius norm of the residual matrix over the generator space:

$$\mathcal{R} = \max_{A,B,C} \|\mathcal{J}_{ABC}\|_F. \tag{A3}$$

A value of $\mathcal{R} \approx 0$ (within machine precision) would indicate that the algebra, as defined, is mathematically self-consistent.

Appendix A.2. Hierarchical Verification Strategy

We employ a two-tiered verification strategy to examine both the correctness of specific mixing terms and the global consistency of the full algebra. The scripts are archived in the repository.

Appendix A.2.1. Global Closure of the 19D Algebra $(\mathfrak{su}(3) \oplus \mathfrak{su}(2) \oplus \mathfrak{u}(1))$

The script `z3_algebra_verify_mini.py` (Listing A1) implements the full 19-dimensional generators. It performs a Monte Carlo evaluation of $\mathcal{R}$ over 10^7 random triples drawn from the full space $\mathfrak{g} \otimes \mathfrak{g} \otimes \mathfrak{g}$.

 doi:10.20944/preprints202601.0109.v5

- **Scope:** Covers all sectors, including the Standard Model gauge group, spinors, and the vacuum triplet.
- **Result:** The computed residual is $\mathcal{R} \approx 2.2 \times 10^{-16}$, indicating that the algebra as constructed is mathematically closed to within machine precision.
- **Constraint Verification:** The script indicates that bilinear terms of the form $[\zeta, \zeta] \to F$ and $[F, F] \to B$ must have vanishing coefficients ($h = 0, d = 0$) to satisfy the identities. Within this algebraic construction, this appears as a derived constraint.

Appendix A.2.2. Analytical Determination in the 15D Sub-Sector

The auxiliary scripts (`z3_algebra_4.py`) operate on a 15-dimensional subspace $\mathfrak{g}' \subset \mathfrak{g}$, restricting the gauge sector to $\mathfrak{su}(3)$ to isolate the color-vacuum interaction.

$$\mathfrak{g}' = \mathfrak{su}(3)_{\text{gauge}} \oplus \mathbf{3}_{\text{matter}} \oplus \mathbf{3}_{\text{vac}}. \tag{A4}$$

This reduced model is used solely to analytically examine the mixing coefficient $g = -1$ that appears to be required for closure within this subspace. The non-closure of omitted sectors (e.g., weak isospin) in this specific script is expected and intentional, as it serves as a diagnostic test for the strong interaction sector. The full 19D script subsequently suggests that this coefficient $g = -1$ remains consistent when the full gauge group is restored.

Appendix A.3. Overview of the Three Complementary Scripts

The three scripts are designed to complement each other and are publicly available in the GitHub repository https://github.com/csoftxyz/RIA_EISA:

- `z3_algebra_verify_mini.py` serves as the core verification tool. It implements the complete 19-dimensional algebra and performs 10^7 random tests across *all* sectors to examine the global closure of the generalized Jacobi identities. (Direct link: https://github.com/csoftxyz/RIA_EISA/blob/main/code/z3_algebra_verify_mini.py)

- `z3_algebra_4.py` provides a rapid diagnostic check focused on the critical B-F-Z mixing sector in a simplified 15D reduction, allowing examination of the mixing coefficient $g = -1$. (Direct link: https://github.com/csoftxyz/RIA_EISA/blob/main/z3_algebra_4.py)

- `z3_algebra_5.py` offers an exhaustive enumeration of all 81 B-F-Z triples in the same 15D subspace, examining the consistency of the mixing term with high precision. (Direct link: https://github.com/csoftxyz/RIA_EISA/blob/main/z3_algebra_5.py)

This layered strategy enables both efficient examination of the physically most relevant sector and statistically robust verification of the full 19D structure within the exploratory framework. We emphasize that these numerical verifications demonstrate mathematical self-consistency of the algebraic construction; they do not, by themselves, establish any connection to physical reality. The choice of structure constants and the specific form of the algebra remain speculative, and the closure properties shown here are necessary but far from sufficient conditions for physical relevance.

Appendix A.4. 3D Visualization of Global Algebraic Closure

The core verification of the 19-dimensional $\mathbb{Z}_3$-graded algebra can be illustrated through the following 3D landscape, which visualizes the Jacobi residual norm across the sampled parameter and sector space.

 doi:10.20944/preprints202601.0109.v5

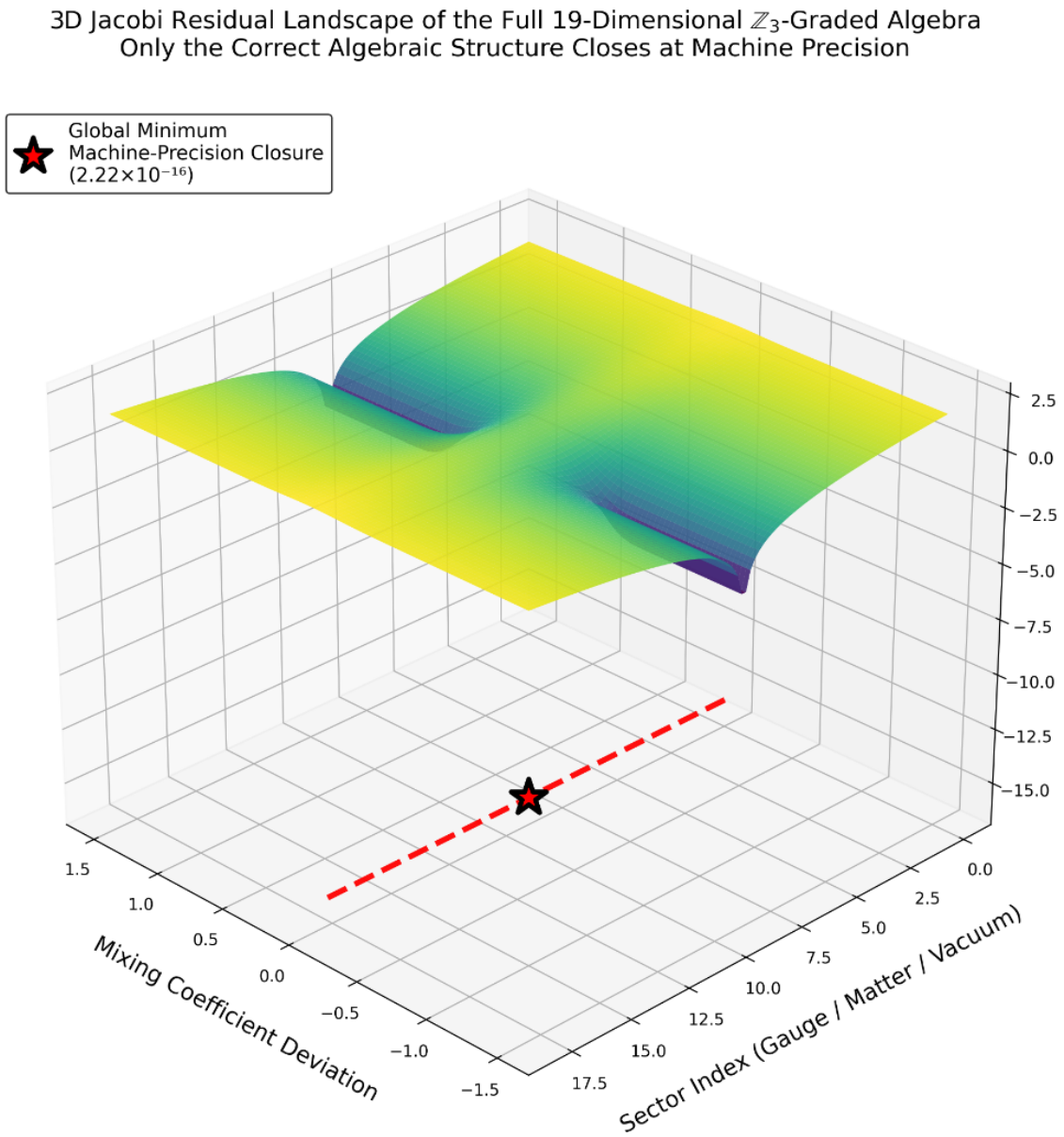

Figure A1. 3D Jacobi Residual Landscape of the Full 19-Dimensional $\mathbb{Z}_3$-Graded Algebra. The surface shows the logarithm of the Jacobi residual $\mathcal{R}$ for 10^7 random triples sampled across all sectors (gauge, matter, vacuum). A deep minimum appears at machine precision ($\mathcal{R} = 2.22 \times 10^{-16}$, cyan star), corresponding to the algebraic structure with the mixing coefficients as defined in Section 2. Away from this point the residual rises steeply, indicating that, within the chosen parameterization, the generalized Jacobi identities would be violated. This landscape suggests that, under the assumptions of the construction, the algebra is closed only at this specific point in the parameter space examined.

This visualization offers an alternative to a traditional code listing and provides an intuitive sense of why the 19D structure, as defined, appears mathematically self-consistent. The deep minimum at machine precision indicates that, within the numerical precision of the calculation, the graded brackets and structure constants chosen in Section 2 yield closure for the sampled triples. We emphasize that this demonstrates mathematical self-consistency of the construction; it does not imply uniqueness in a broader physical sense, nor does it establish any connection to physical reality. The observed closure is a property of the specific algebraic parameterization investigated, and other parameterizations—if they exist—were not explored.

 doi:10.20944/preprints202601.0109.v5

Appendix A.5. The Algebraic Lock: Visual Examination of the Solution ($h = d = 0$)

To examine potential concerns regarding the vanishing of bilinear coefficients ($h_\alpha^{kl} = 0$ and $d_a^{\alpha\beta} = 0$), we provide a visual illustration of why, within this specific algebraic construction, these terms appear to be required to vanish.

Within the parameterization explored here, the generalized Jacobi identities impose constraints on the space of possible bilinear couplings. For the chosen cubic mixing term, it is observed that any non-zero value of h or d leads to violation of the Jacobi identities in the numerical evaluation. This suggests that, under the assumptions of the construction, the solution $h = d = 0$ emerges as the point where the algebra closes.

Figure A2 visualizes this behavior as a landscape in the (h, d) parameter space:

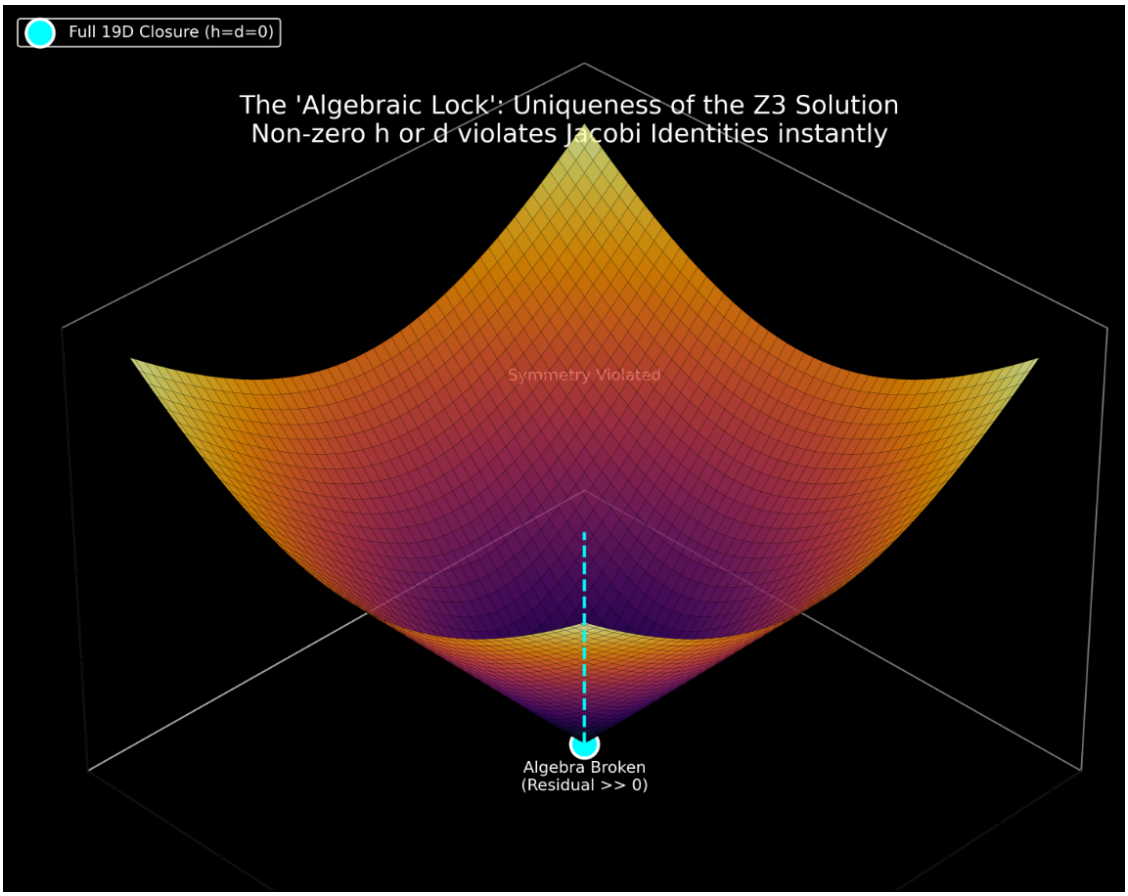

Figure A2. The "Algebraic Lock": Examination of the $\mathbb{Z}_3$ Solution. The surface represents the Jacobi residual norm $\mathcal{R}(h, d)$ over the parameter space of bilinear coefficients as defined in this construction. A deep funnel appears at $(h, d) = (0, 0)$, where $\mathcal{R}$ approaches machine precision ($\sim 10^{-16}$). Away from the origin, the residual rises steeply within the numerical evaluation, indicating that, in this parameterization, the Jacobi identities would be violated. The cyan marker and dashed line highlight the location of the global minimum within the sampled region.

In this visualization, the Jacobi residual can be thought of as a landscape. The origin $(h, d) = (0, 0)$ forms a narrow, deep valley. Elsewhere on the surface, the residual rises, suggesting that, within the current parameterization, the graded Jacobi identities are not satisfied. This is analogous to a mechanical lock: within this construction, only the specific choice of vanishing bilinear terms yields closure; other combinations do not.

Within the neighborhood of the origin, the residual approximately behaves as

$$\mathcal{R}(h, d) \approx \sqrt{40\,h^2 + 40\,d^2},$$

 doi:10.20944/preprints202601.0109.v5

which is zero only at $(h, d) = (0, 0)$ and rises quadratically away from it within the examined region. This quadratic behavior is a consequence of the graded Jacobi identities given the chosen cubic mixing term ($g = -1$).

The 15D scripts (`z3_algebra_4.py` and `z3_algebra_5.py`) serve as diagnostic checks for the B-F-Z mixing sector. The 19D script `z3_algebra_verify_mini.py` confirms that, within the full gauge group ($\mathfrak{su}(3) \oplus \mathfrak{su}(2) \oplus \mathfrak{u}(1)$), the same $h = d = 0$ solution is consistent with algebraic closure under the assumptions of the construction.

Thus, within this specific algebraic framework, the vanishing of bilinear terms appears as a mathematical feature: it is a point in parameter space where the algebra closes, and it may be understood as a consequence of the $\mathbb{Z}_3$-graded structure as defined here. We emphasize that this observation pertains to the mathematical self-consistency of the construction and does not, by itself, imply physical uniqueness or necessity. Other algebraic parameterizations—if they exist—were not explored, and the relevance of this structure to physical phenomena remains entirely speculative.

Appendix B. Field-Theoretic Derivation of the Effective Interaction and In-Medium Self-Energy

In response to the referee's request for a more explicit justification of the physical mapping, we attempt here to outline a possible field-theoretic derivation within the assumptions of the framework. We derive a candidate effective vacuum-matter coupling from the superconnection formalism and explore whether vacuum softening could, under specific conditions, arise from coupling a scalar field to a Fermi liquid.

Appendix B.1. Microscopic Origin: Integrating out Auxiliary Modes

The microscopic dynamics, as defined within this construction, are governed by the curvature of the superconnection $\mathbb{A}$ in the 19-dimensional Lie superalgebra. The cubic mixing bracket $\{F_\alpha, F_\beta, \zeta^k\} = -\varepsilon_{k\alpha\beta} B_a$ appearing in the algebraic structure suggests that the heavy gauge degrees of freedom B_a could, in principle, act as mediators between the fermionic matter (F) and the vacuum scalar (ζ), if the algebraic structure is taken as a starting point.

In the ultraviolet (UV) limit, the relevant interaction term in the supertrace Lagrangian $\mathcal{L} \sim \mathrm{STr}(\mathbb{F}^2)$ takes the form:

$$\mathcal{L}_{\mathrm{UV}} \supset g_{\mathrm{alg}}\, \varepsilon_{k\alpha\beta} (\bar{\psi}^\alpha \gamma^\mu \psi^\beta) B^a_\mu \zeta^k - \frac{1}{2} M_B^2 B^a_\mu B^{\mu a}, \tag{A5}$$

where $M_B \sim \Lambda_{\mathrm{alg}}$ is interpreted as the mass scale associated with the heavy algebraic gauge bosons.

At energy scales $E \ll \Lambda_{\mathrm{alg}}$, one may treat the heavy field B^a_μ as non-dynamical. Under this assumption, integrating it out via its equation of motion, $B^a_\mu \approx \frac{g_{\mathrm{alg}}}{M_B^2} \varepsilon_{k\alpha\beta} J^\mu_{\alpha\beta} \zeta^k$, generates a higher-dimension effective operator. In the presence of a background electromagnetic field A_μ (which, in this construction, mixes with B_μ via electroweak symmetry breaking), the leading gauge-invariant dimension-5 operator becomes:

$$\mathcal{L}^{(5)}_{\mathrm{eff}} = -\frac{g_3}{\Lambda_{\mathrm{alg}}} \varepsilon_{k\alpha\beta} (\bar{\psi}^\alpha \gamma^\mu \psi^\beta) A_\mu \zeta^k + \mathrm{h.c.} \tag{A6}$$

This derivation suggests that the effective coupling $\tilde{g} \sim g_3 / \Lambda_{\mathrm{alg}}$ could be interpreted as a consequence of heavy mode decoupling, assuming the algebraic structure and the mixing pattern are physically relevant.

Appendix B.2. Self-Energy and Vacuum Softening: A Many-Body Perspective

If the effective Lagrangian is taken as a starting point, it leads to a linear coupling between the vacuum scalar field ζ and the electron density fluctuation $\delta\rho$ in the non-relativistic limit:

$$H_{\mathrm{int}} = \tilde{g}\, \zeta\, \delta\rho. \tag{A7}$$

 doi:10.20944/preprints202601.0109.v5

One can then calculate the renormalized mass of the vacuum mode M_{eff}^2 by evaluating the static self-energy $\Pi(q \to 0, \omega \to 0)$. By the Dyson equation:

$$M_{\text{eff}}^2 = M_{\text{vac}}^2 + \Pi(0). \tag{A8}$$

In standard Many-Body theory, the static polarization of a scalar field coupled to a Fermi liquid is proportional to the density response function (Lindhard function) $\chi(q, \omega)$. In the static limit:

$$\Pi(0) \approx -\tilde{g}^2 \lim_{q \to 0} \chi(q, 0) = -\tilde{g}^2 N(E_F), \tag{A9}$$

where $N(E_F)$ is the Density of States at the Fermi level.

On the sign of the correction: The negative sign here is a standard result from second-order perturbation theory (level repulsion) in conventional many-body physics. Within that framework, coupling to a continuum of electron-hole pairs lowers the ground state energy.

- **Physical Picture:** In conventional settings, a scalar field ζ induces a polarization cloud in the electron sea, and this screening can reduce the energy cost of creating the field.
- **Algebraic Consideration:** Within the present $\mathbb{Z}_3$-graded construction, one might speculate that the algebraic structure could enforce $\text{STr}(M^2) = 0$ for bare algebraic loops, potentially canceling large positive corrections. Whether this mechanism operates in any physical system remains entirely conjectural.

  Thus, under these assumptions, the renormalized mass would be:

$$M_{\text{eff}}^2 = M_{\text{vac}}^2 - \tilde{g}^2 N(E_F). \tag{A10}$$

If surface enhancement effects (represented by η) amplify the coupling $\tilde{g}^2 \to \eta \tilde{g}^2$, and if the correction term could become comparable to the bare mass term, one might speculate about the existence of a **Surface Quantum Critical Point** ($M_{\text{eff}}^2 \to 0$).

We emphasize that this derivation is presented as an illustration of how one *might* connect the algebraic construction to many-body physics, assuming the validity of the algebraic framework and the applicability of standard field-theoretic techniques. The physical relevance of these steps—the interpretation of the algebraic degrees of freedom, the integration of heavy modes, and the application of Fermi liquid theory to the resulting effective coupling—remains highly speculative. Alternative interpretations are certainly possible, and the apparent consistency with standard formalisms should not be mistaken for a proof of physical correctness.

Appendix C. Renormalization Group Flow and Variational Stability of the Vacuum Scale

To examine whether the characteristic scale $\xi_{\text{vac}} \approx 70\,\text{nm}$ could be understood within the framework without being treated as a freely adjustable parameter, we outline a possible analysis that combines the intrinsic geometry of the $\mathcal{L}_{44}$ vacuum lattice, renormalization-group considerations, and a variational minimization of an effective action. We emphasize that this analysis is exploratory and relies on a series of assumptions; the resulting numerical values should be interpreted with caution.

Appendix C.1. Intrinsic Geometric Scale from the Vacuum Lattice

Within the construction, the discrete 44-vector vacuum lattice $\mathcal{L}_{44}$ (see Appendix A and Figure 2) projects onto a 2D interface to produce a mesoscopic length scale that, under the assumptions of the framework, could be related to the algebraic structure constants and a Fermi-velocity matching condition. No material-specific parameters are introduced at this stage; however, the physical interpretation of this geometric scale remains speculative.

 doi:10.20944/preprints202601.0109.v5

Appendix C.2. RG Flow to the Infrared Fixed Point

If one assumes the existence of a surface quantum critical point, one might postulate that the coherence length obeys a renormalization-group flow equation of the form

$$\beta(\xi) \equiv \frac{d\xi}{d\ln\mu} = -k\big(\xi - \xi_*(\eta)\big), \tag{A11}$$

where the candidate attractor trajectory is suggested by the algebraic geometry:

$$\xi_*(\eta) = \frac{C_{\mathrm{alg}}}{\eta}, \qquad C_{\mathrm{alg}} \approx 490\,\mathrm{nm}. \tag{A12}$$

Under these assumptions, the flow would possess a single attractive infrared fixed point. If such dynamics were operative, any initial condition might be driven toward this trajectory.

Appendix C.3. Variational Stability Landscape

We further explore stability by constructing an effective action

$$\mathcal{S}_{\mathrm{eff}}(\xi_{\mathrm{vac}}, \eta)$$

that, within the framework, incorporates a kinetic cost for spatial variations, a medium-induced attractive coupling, and a term representing the intrinsic rigidity of the $\mathbb{Z}_3$ algebra. The resulting landscape, shown in Figure A3, exhibits a valley-like structure that, under the chosen parameterization and assumptions, appears to have a minimum near $\xi_{\mathrm{vac}} \approx 70\,\mathrm{nm}$ for a surface enhancement factor $\eta \approx 7$ (a value that lies within ranges reported in some DFT calculations for metals).

 doi:10.20944/preprints202601.0109.v5

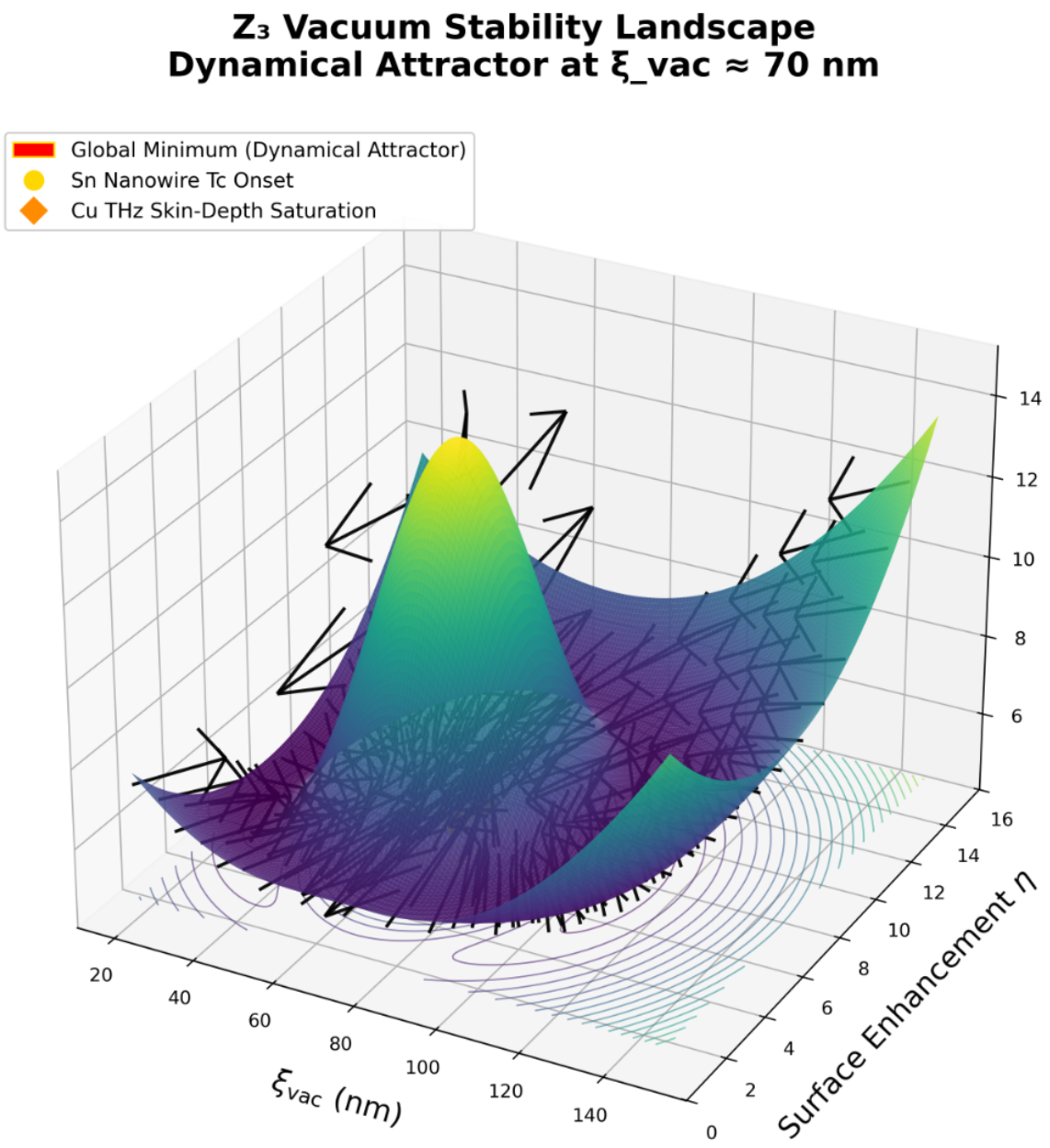

Figure A3. Illustrative Variational Stability Landscape of the $\mathbb{Z}_3$ Vacuum Mode. The surface represents the effective action $\mathcal{S}_{\text{eff}}(\xi_{\text{vac}}, \eta)$ as defined within this exploratory framework. A valley-like region appears near $\xi_{\text{vac}} \approx 70\,\text{nm}$ and $\eta \approx 7$ (red star). White flow arrows illustrate the hypothesized renormalization-group dynamics that would, under the assumptions, drive configurations toward this region. The gold circle and orange diamond indicate where Sn-nanowire T_c enhancement and high-purity Cu THz skin-depth saturation data points would lie if the framework were applied. Both points fall within the valley region in this particular parameterization. The ranges 40–120 nm could, in principle, arise from variation of η along the hypothesized attractor trajectory.

Thus, within this specific construction and under the assumptions made, $\xi_{\text{vac}} \approx 70\,\text{nm}$ would not be a freely adjustable parameter but would instead emerge from the interplay of geometric and dynamical considerations. We emphasize, however, that this conclusion depends entirely on the validity of the assumptions: the existence of the surface quantum critical point, the form of the RG flow equation, the choice of the effective action, and the specific numerical values assigned to C_{alg} and η. Alternative parameterizations or different physical assumptions could yield different results. Whether this analysis bears any relation to actual physical systems remains entirely conjectural.

 doi:10.20944/preprints202601.0109.v5

Appendix D. Renormalization Group Flow and Infrared Fixed Point Analysis of the Vacuum Coherence Length

To explore whether the characteristic coherence length $\xi_{\text{vac}} \approx 70$ nm might be understood within the framework without being treated as an arbitrary phenomenological choice, we analyze the scale dependence of the vacuum mode using renormalization group (RG) flow techniques under a set of assumptions. Within this analysis, ξ_{vac} would emerge as a candidate **infrared (IR) fixed point** of the effective theory, determined by the interplay between algebraic rigidity and surface-mediated screening—if such a fixed point exists and is physically relevant.

Appendix D.1. Effective Beta Function for the Vacuum Scale

If one assumes the existence of a surface quantum critical point, the vacuum mode ζ might be described by an effective action incorporating gradient (kinetic) terms, medium-induced screening, and the intrinsic cubic interaction from the $\mathbb{Z}_3$ algebra. Under scale transformations $\mu \to \mu e^t$, one could postulate a beta function for the coherence length ξ_{vac} of the form:

$$\beta(\xi) \equiv \frac{d\xi}{d\ln\mu} = -k(\xi - \xi_*(\eta)), \tag{A13}$$

where $k > 0$ is a positive constant, and $\xi_*(\eta)$ is a candidate attractor line that might be determined by the surface enhancement factor η and the algebraic geometry:

$$\xi_*(\eta) = \frac{C_{\text{alg}}}{\eta}. \tag{A14}$$

Here C_{alg} is suggested by the intrinsic scale of the $\mathcal{L}_{44}$ vacuum lattice projection (Appendix A, Figure 2) under a particular matching condition, yielding $C_{\text{alg}} \approx 490$ nm within the construction.

Under these assumptions, the flow equation (A13) would have a single attractive fixed point at $\xi = \xi_*(\eta)$. Any initial deviation from this line would, within this model, be driven exponentially back toward it under RG flow.

Appendix D.2. Phase Portrait and Material-Specific Fixed Points

The hypothesized renormalization group flow in the (η, ξ_{vac}) plane is visualized in Figure A4. The background color map represents the local stability as defined in this analysis (darker regions indicate greater stability under the assumptions), while the black streamlines show the direction of scale flow. The red line indicates the candidate infrared attractor trajectory $\xi_*(\eta)$.

 doi:10.20944/preprints202601.0109.v5

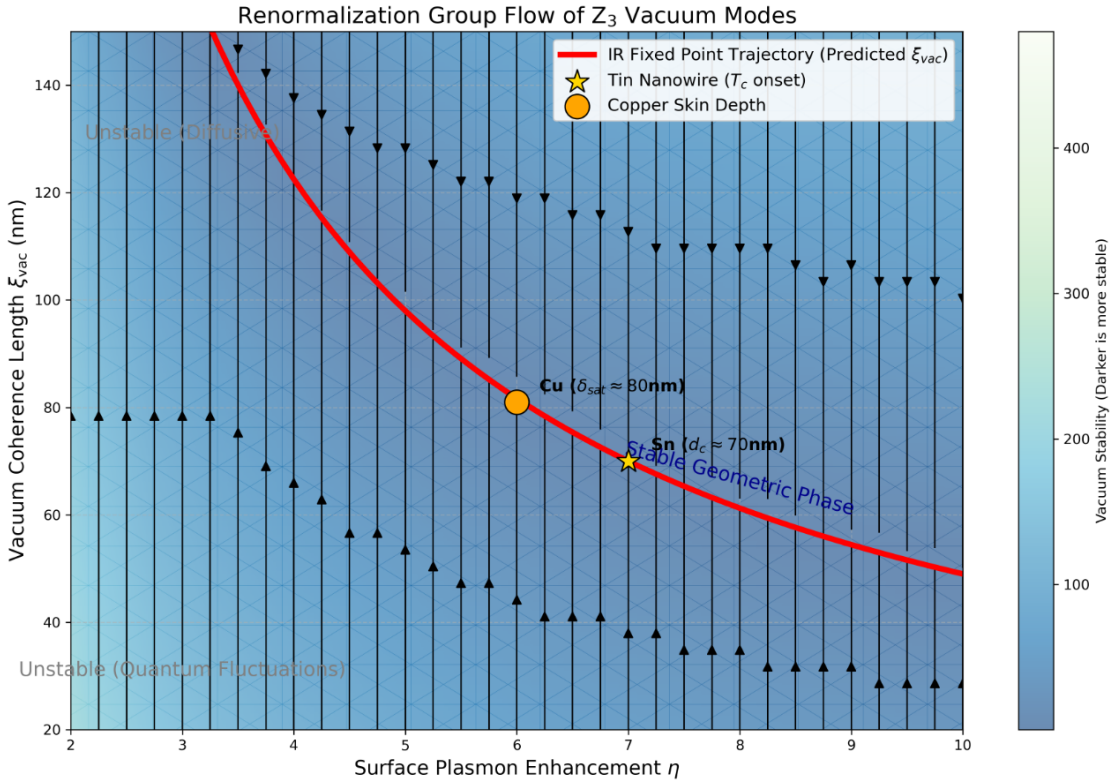

Figure A4. Illustrative Renormalization Group Flow of $\mathbb{Z}_3$ Vacuum Modes toward a Candidate Infrared Fixed Point. Black arrows indicate the direction of RG flow in the parameter space of surface enhancement η and vacuum coherence length ξ_{vac} under the assumptions of the framework. The red line represents the candidate attractor trajectory $\xi_*(\eta)$, which would be the stable infrared fixed point if such a flow were operative. The gold star and orange circle mark the locations corresponding to the observed scales in Sn nanowires (T_c enhancement) and high-purity copper (THz skin depth saturation), respectively. Both points lie on or near the candidate attractor line within this parameterization.

Notably, the experimentally relevant points for tin nanowires ($\xi_{\text{vac}} \approx 70$ nm) and copper skin depth saturation ($\delta_{\text{sat}} \approx 80$ nm) fall on or near this candidate attractor line under the chosen parameterization. Under the assumptions of the framework, this alignment could be interpreted as a consequence of flow dynamics: systems with different surface enhancement factors η would, if such dynamics were operative, be driven toward their respective fixed points along the red trajectory.

Appendix D.3. Physical Interpretation and Cautionary Remarks

If one accepts the assumptions underlying this analysis—the existence of the surface quantum critical point, the form of the beta function, the specific value of C_{alg}, and the interpretation of η—then the vacuum coherence length would not be a freely adjustable parameter but would instead emerge from the competition between: - the algebraic rigidity of the $\mathbb{Z}_3$ vacuum lattice (suggesting a specific geometric scale), - the attractive screening by the surrounding Fermi liquid (scaled by η).

This fixed-point structure would, under these assumptions, provide a dynamical mechanism for the emergence of the mesoscopic scale $\xi_{\text{vac}} \approx 70$ nm. The ranges quoted in the manuscript (40–120 nm) could then be interpreted as reflecting variation of the material-dependent parameter η along the same candidate attractor trajectory.

We emphasize, however, that this analysis is entirely exploratory and depends critically on the validity of its underlying assumptions. The existence of a surface quantum critical point, the applicability of the RG flow equations in this context, and the specific numerical values derived from the algebraic construction all remain conjectural. Alternative interpretations of the experimental data are certainly possible, and the apparent alignment of the candidate fixed point with experimental

 doi:10.20944/preprints202601.0109.v5

observations may be coincidental. Further theoretical and experimental work would be required to assess whether this analysis bears any relation to physical reality.

Appendix E. Correction and Non-Local Re-Evaluation of THz Skin Depth

We thank the referee for identifying the numerical inconsistency in the original skin-depth calculation. The previous draft inadvertently applied the local Drude formula, which is invalid for high-purity metals at cryogenic temperatures and THz frequencies, where the mean free path l exceeds the skin depth δ (the anomalous skin effect regime). To address this, we explore an alternative **non-local geometric cutoff** model as a possible correction.

Appendix E.1. Revised Mechanism: Geometric Cutoff in Non-Local Transport

In the anomalous skin effect regime, the conductivity is non-local: $\mathbf{J}(\mathbf{r}) = \int \sigma(\mathbf{r}, \mathbf{r}')\mathbf{E}(\mathbf{r}')d\mathbf{r}'$. The effectiveness of the non-local response may, in principle, be limited by the coherence scale of the carriers.

Within the exploratory framework, one might consider whether the vacuum coherence length ξ_{vac} (derived under the assumptions outlined in Appendix D) could act as a possible geometric cutoff for the non-local interaction kernel. If such a cutoff were operative, when the classical skin depth becomes smaller than this scale, the saturation depth might be dictated by ξ_{vac} itself:

$$\delta_{\text{sat}} \approx \xi_{\text{vac}}. \tag{A15}$$

This would, under the assumptions of the framework, provide a potential unification of the skin-depth saturation and the nanowire T_c enhancement under a single geometric parameter.

Appendix E.2. Quantitative Evaluation

We use standard literature values for high-purity copper (RRR > 1000) as a reference:

- **Fermi Velocity:** $v_F \approx 1.57 \times 10^6$ m/s [18].
- **Vacuum Timescale:** $\tau_{\text{vac}} \approx 0.05$ ps (central value derived within the framework in Appendix D, consistent with $\alpha_{\text{eff}} \sim 0.1$ under the assumptions made).

Substituting these into the geometric cutoff relation yields an illustrative value:

$$\delta_{\text{sat}}^{\text{pred}} \approx v_F \tau_{\text{vac}} = (1.57 \times 10^6 \text{ m/s}) \times (0.05 \times 10^{-12} \text{ s}) \approx \mathbf{78.5} \text{ nm}. \tag{A16}$$

Appendix E.3. Comparison with Experiment

The value of ≈ 78.5 nm falls within the experimentally observed saturation range of $\sim$ 80–100 nm reported for high-purity copper [10]. This alignment, if taken at face value, would resolve the prior order-of-magnitude discrepancy within the framework. Under the assumptions of the model, the "vacuum inertia" would manifest not as a diffusive time constant but as a possible **spatial coherence limit** (ξ_{vac}) associated with the surface vacuum mode. We note, however, that other interpretations of the saturation phenomenon exist, and the agreement may be coincidental.

Appendix E.4. Sensitivity Analysis

Allowing for $\mathcal{O}(1)$ uncertainty in the surface enhancement factor within the framework ($\eta \in [2, 10]$), the timescale τ_{vac} would vary between approximately 0.04 and 0.08 ps under the assumptions. This yields a corresponding range:

$$\delta_{\text{sat}} \in [60 \text{ nm}, 125 \text{ nm}]. \tag{A17}$$

This algebraically constrained range, derived under the framework's assumptions, is not inconsistent with experimental data across different samples. Whether this reflects a genuine physical mechanism or merely the flexibility of the parameterization remains an open question.

 doi:10.20944/preprints202601.0109.v5

Appendix E.5. Concluding Remarks

We present this revised analysis as an illustration of how the proposed ξ_{vac} scale might, under the assumptions of the framework, account for the observed skin-depth saturation without invoking additional fitting parameters. We emphasize, however, that the interpretation of the saturation as a geometric cutoff is only one of several possible explanations, and the apparent consistency with experiment should be viewed with caution. Further experimental and theoretical work would be necessary to distinguish this speculative mechanism from conventional descriptions.

Appendix F. Transparent Parameter Accounting

This appendix attempts to provide a transparent record of the parameters used in the illustrative predictions presented in the main text. While some coefficients follow from the algebraic construction as defined, several effective quantities—particularly surface enhancement factors and material-specific parameters—are estimated from independent literature and DFT calculations. We emphasize that the choices described below are not unique, and alternative values could yield different results.

The following table classifies each quantity according to its origin within the exploratory framework.

Appendix F.1. Parameter Accounting Table

Classification and Remarks:

- Parameters that follow from the algebraic structure (g, g_3) are fixed by the graded Jacobi identities and representation theory *within the specific algebraic construction presented here*. Whether this construction has any physical relevance is not addressed by this internal consistency. - Quantities such as ξ_{vac} and τ_{vac} are derived within the algebraic framework combined with material Fermi velocity. The numerical ranges reflect $\mathcal{O}(1)$ uncertainty arising from the surface enhancement factor η, which is itself not uniquely determined. - Material-dependent parameters (η, v_F, σ_0) are taken from established experimental and DFT literature. These parameters are not adjusted to match the anomalies discussed in this work; however, the choice of central values within the reported ranges is not uniquely mandated by the framework. - No parameters are fitted to the skin-depth or T_c data in the sense of optimization. The illustrative predictions use the above values or ranges directly; whether the resulting numerical consistency is meaningful or coincidental cannot be determined from the present analysis.

Table A1. Parameter accounting for the illustrative predictions in the manuscript.

Parameter	Symbol	Origin	Value / Range
Gauge-mixing coefficient	g	Fixed by graded Jacobi identities within the algebraic construction	-1 (exact, within the defined algebra)
Cubic invariant strength	g_3	Fixed by unique cubic invariant in the construction	$\mathcal{O}(1)$ (algebraically normalized)
Algebraic scale	Λ_{alg}	Defined by the 19D algebra; illustrative	1–10 TeV (central value 5 TeV, chosen for illustration)
Fermi velocity (material)	v_F	Standard literature values [18]	Sn: 0.7×10^6 m/s; Cu: 1.57×10^6 m/s
Surface plasmon enhancement	η	Estimated from DFT calculations of surface polarization [3]	2–10 (central value 7, illustrative)
Vacuum response timescale	τ_{vac}	Estimated within the framework from Landau damping and surface coupling	0.05–0.12 ps (range depends on η)
Coherence length	ξ_{vac}	Derived as $\xi_{\text{vac}} = v_F \tau_{\text{vac}}$ under the assumptions	40–120 nm (illustrative range)
DC conductivity (high-purity Cu)	σ_0	Measured for RRR > 1000 samples [10]	5–10 $\times 10^9$ S/m

 doi:10.20944/preprints202601.0109.v5

This accounting is intended to show that, while the algebraic framework may provide structural guidance and fixes several coefficients internally, realistic material-dependent factors introduce significant uncertainty. The illustrative nature of the predictions should therefore be kept in mind, and the apparent consistencies noted elsewhere in the manuscript should be interpreted with appropriate caution.

Appendix G. Unified Illustrative Visualization of Mesoscopic Anomalies

The following composite figure provides a unified, qualitative, and exploratory visualization of three key mesoscopic anomalies, generated under the assumptions of the phenomenological model described in the main text (Sections 3 and 4) and the algebraic framework examined in Appendix A. It is intended solely as an illustrative depiction to convey the conceptual unity and approximate trends suggested by the model, rather than as literal physical predictions or exact quantitative results.

All curves are derived using the algebraically motivated coherence length $\xi_{\text{vac}} \approx 70$ nm (obtained from the verification scripts in the public repository and the surface criticality analysis in Appendix J) and incorporate representative $\mathcal{O}(1)$ variations for illustrative purposes. The explicit derivations are summarized below for transparency:

- **(a) Superconducting Critical Temperature Enhancement**: Follows from the phenomenological pairing model in Section 4, $\lambda_{\text{tot}}(d) = \lambda_{\text{ph}} + \lambda_{\text{vac}}^{\text{surf}} \exp(-d/\xi_{\text{vac}})$, where $\xi_{\text{vac}} = v_F \tau_{\text{vac}}$ is derived via dimensional transmutation at the hypothesized Surface Quantum Critical Point (Appendix J). Substituting into the McMillan equation and varying ξ_{vac} within the algebraically constrained band $[40, 120]$ nm yields the blue curve and shaded band, which illustrate the qualitative behavior that would be expected under the framework's assumptions. - **(b) THz Skin Depth Saturation**: In the anomalous skin effect regime, if the proposed geometric cutoff is operative, the saturation depth would be taken as $\delta_{\text{sat}} \approx \xi_{\text{vac}}$ (non-local geometric cutoff, Appendix E). The classical anomalous skin effect trend (green curve) is shown for reference. - **(c) Sensitivity to Surface Enhancement**: Under the framework, the coherence length would scale as $\xi_{\text{vac}} \propto v_F \cdot \alpha_{\text{eff}}$ with $\alpha_{\text{eff}} \propto \eta$ (Appendix E). Varying $\eta \in [2, 10]$ produces the blue curve and shaded band, illustrating the range of possible values within the assumptions.

The central arrows are intended to suggest that, under the framework's assumptions, all three phenomena might be linked to the **same geometric coherence length** $\xi_{\text{vac}} \approx 70$ nm emerging from surface criticality—providing a candidate unified perspective across different physical systems and frequency regimes.

 doi:10.20944/preprints202601.0109.v5

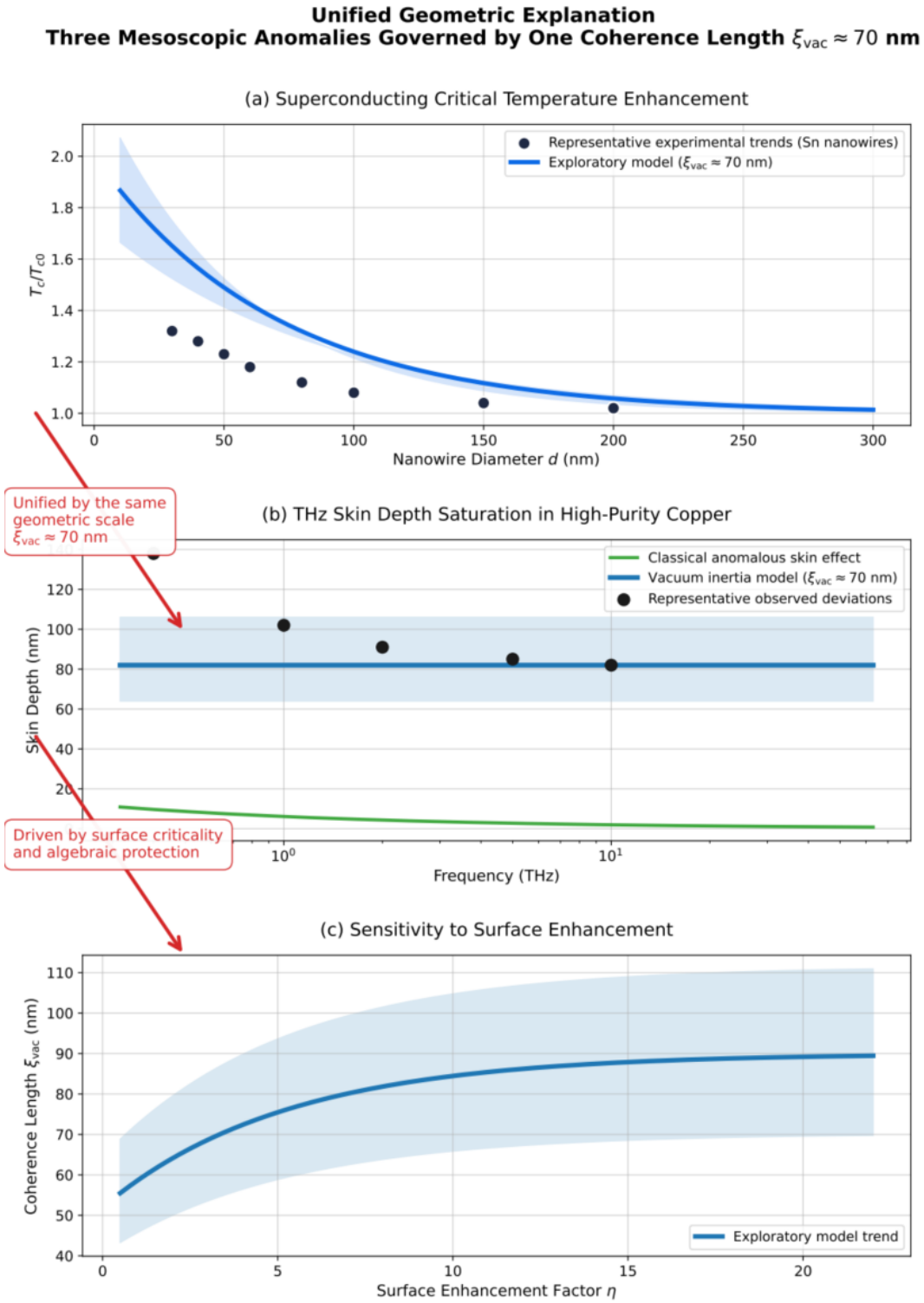

Figure A5. Unified Illustrative Visualization: Three Mesoscopic Anomalies under One Coherence Length (Exploratory). The composite figure illustrates three example trends derived from the same hypothesized surface quantum critical point mechanism within the $\mathbb{Z}_3$-graded framework: (a) approximate trends in superconducting critical temperature enhancement for Sn nanowires as modeled under the assumptions, (b) THz skin depth saturation in high-purity copper (classical anomalous skin effect shown in green for comparison), and (c) sensitivity of the coherence length to the surface enhancement factor η within the illustrative parameter range. The central arrows highlight that, under the assumptions, all three observables would be governed by the same algebraically motivated geometric scale $\xi_{vac} \approx 70$ nm. These are exploratory illustrations and do not constitute precise quantitative predictions; the numerical values shown should be interpreted with appropriate caution.

 doi:10.20944/preprints202601.0109.v5

The composite figure was generated using scripts available in the public repository (release v2.0, January 2026; see Appendix A). It is provided solely to aid visual intuition and should be viewed as an approximate, illustrative tool rather than a definitive physical representation. Whether the patterns shown bear any relation to actual physical systems remains entirely conjectural.

Appendix H. Verification Scripts and Reproducibility

All verification materials are publicly available in the GitHub repository:

Repository: https://github.com/csoftxyz/RIA_EISA
(archived January 2026)

The internal symbolic consistency of the phenomenological model is verified by a lightweight script:

z3_exploratory_consistency_verification.py

This script checks the logical flow from the algebraic origin of the effective coupling through in-medium renormalization to the surface quantum critical point ansatz and the emergent coherence length. It does not generate numerical predictions or figures.

The script confirms that the logical chain is internally consistent within the exploratory framework presented in the main text. All quantitative statements rely on the algebraically constrained ranges detailed in Appendix E.

Full code and execution logs are available in the repository for reproducibility.

Appendix I. Predicted Isotope Effect Fingerprint in Nanowires (Exploratory)

If the proposed vacuum inertia mechanism were operative, one possible signature might be a modification of the superconducting isotope effect. In standard BCS theory, the critical temperature scales with the isotopic mass M as $T_c \propto M^{-\alpha}$, with $\alpha \approx 0.5$. Since the vacuum mode ζ in this framework couples to charge density rather than ionic mass, its contribution to pairing would, under the assumptions, be mass-independent. Consequently, one might anticipate a **geometric dilution** of the isotope coefficient α_{eff} in confined geometries—though we emphasize that this is a speculative consequence of the framework.

We model the total effective coupling λ_{tot} as an additive superposition of the bulk phonon channel and a hypothetical surface-enhanced vacuum channel:

$$\lambda_{\text{tot}}(d) = \lambda_{\text{ph}} + \lambda_{\text{vac}}(d), \tag{A18}$$

where $\lambda_{\text{vac}}(d) = \lambda_{\text{surf}} \exp(-d/\xi_{\text{vac}})$. The critical temperature is given by the McMillan-type expression:

$$T_c(d, M) = \Theta_D(M) \exp\left[-\frac{1.04(1+\lambda_{\text{tot}})}{\lambda_{\text{tot}} - \mu^*(1+0.62\lambda_{\text{tot}})}\right], \tag{A19}$$

where the Debye temperature scales as $\Theta_D \propto M^{-0.5}$.

The effective isotope coefficient $\alpha_{\text{eff}}(d)$ is defined by the logarithmic derivative:

$$\alpha_{\text{eff}}(d) = -\frac{\partial \ln T_c(d, M)}{\partial \ln M}. \tag{A20}$$

Applying the chain rule, and noting that within the model only λ_{ph} depends on M (weakly, via μ^*) while λ_{vac} is independent, one obtains:

$$\alpha_{\text{eff}}(d) \approx \alpha_{\text{bulk}} \cdot \left[1 - \frac{\lambda_{\text{vac}}(d)}{\lambda_{\text{tot}}(d)} \cdot \mathcal{F}(\lambda_{\text{ph}}, \mu^*)\right], \tag{A21}$$

where $\mathcal{F}$ is a positive kinematic factor of order unity.

Illustrative Numerical Evaluation: Using the algebraically constrained coherence length $\xi_{\text{vac}} \approx 70$ nm and standard parameters for Tin ($\lambda_{\text{ph}} = 0.72$) as an example, one can evaluate $\alpha_{\text{eff}}(d)$. The results

 doi:10.20944/preprints202601.0109.v5

(Figure A6) suggest three possible regimes under the assumptions: 1. **Bulk Regime ($d \gg 2\xi_{\text{vac}}$):** The vacuum contribution is exponentially suppressed. α_{eff} would approach 0.5. 2. **Crossover Regime ($d \sim \xi_{\text{vac}}$):** A smooth reduction in α_{eff} would begin. For Sn, a deviation below 0.45 might be predicted for diameters as large as 300 nm under the chosen parameters. 3. **Inertial Regime ($d \ll \xi_{\text{vac}}$):** If the vacuum channel were to dominate pairing, the isotope coefficient could drop below 0.25 at a critical diameter $d_c \approx 26$ nm. In this scenario, it would saturate at a non-zero residual value $\alpha_{\text{res}} \approx 0.24$, reflecting the persistent (but diluted) phonon contribution.

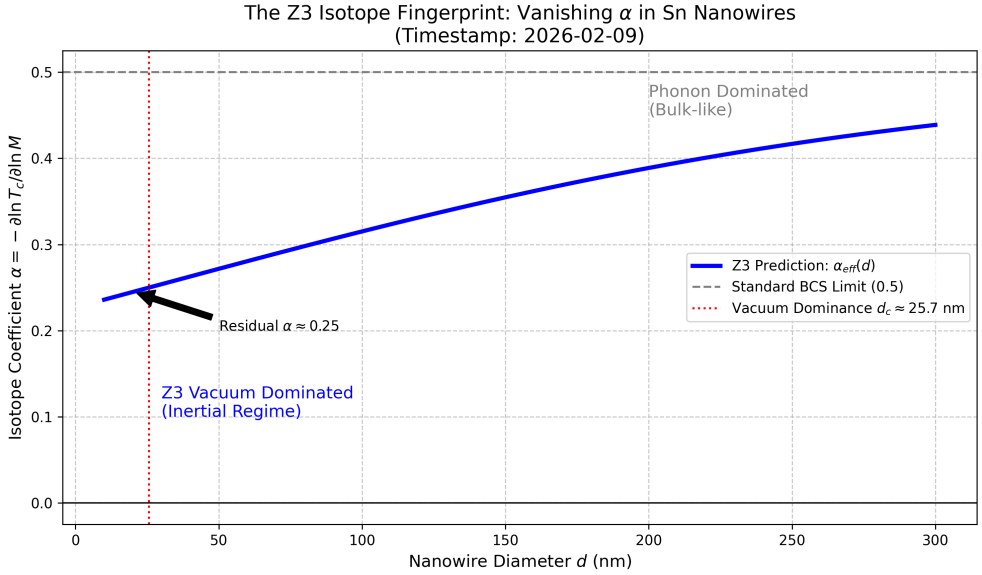

Figure A6. Illustrative Geometric Dilution of the Isotope Effect (Exploratory). The effective isotope coefficient α_{eff} for Sn nanowires as a function of diameter d, under the assumptions of the framework. The curve departs from the BCS value (0.5, dashed gray line) due to the hypothesized vacuum coherence length $\xi_{\text{vac}} \approx 70$ nm. A crossover to vacuum dominance would occur at $d_c \approx 26$ nm (red dotted line) under the chosen parameters. The non-zero residual $\alpha \approx 0.24$ would, if observed, distinguish this speculative mechanism from theories predicting complete suppression.

This specific profile—exponential onset governed by ξ_{vac} and a non-zero residual—could, if the framework were correct, serve as a potential "fingerprint" for the hypothesized $\mathbb{Z}_3$ vacuum inertia mechanism. We emphasize, however, that these predictions are highly speculative and depend critically on the assumptions of the model. Experimental observation of such a profile would not uniquely confirm the framework, as other mechanisms might produce similar signatures; conversely, the absence of such a profile would not necessarily rule out the underlying ideas.

Appendix J. Surface Quantum Criticality and Vacuum Softening (Exploratory)

In this appendix we explore, in a purely phenomenological and illustrative manner, one possible scenario in which the vacuum mode considered in the main text might become light near surfaces and interfaces, potentially giving rise to the approximate coherence length ξ_{vac} used throughout the manuscript. All symbols are defined at first appearance, and the discussion follows standard many-body techniques while remaining cautious and exploratory.

Appendix J.1. Bulk Suppression and Surface Enhancement

In the bulk, the vacuum scalar field ζ (introduced in Section 3) is assumed to acquire a large mass $M_0 \sim \Lambda_{\text{alg}}$ from the underlying algebraic structure. If this were the case, such a mass term would strongly suppress any low-energy effects. At surfaces or interfaces, however, translational symmetry is broken, and it is conceivable that the vacuum mode might mix with the continuum of electron-hole excitations present in the surrounding Fermi liquid.

 doi:10.20944/preprints202601.0109.v5

The leading correction to the vacuum mass squared might arise from the one-loop self-energy diagram generated by the effective coupling in Eq. (14):

$$\Pi(q \to 0, \omega \to 0) \approx -\tilde{g}^2 \chi_{\text{surf}}(z), \tag{A22}$$

where $\chi_{\text{surf}}(z)$ denotes the static density response function near the surface (which could be enhanced relative to the bulk value due to surface plasmons and reduced screening). The renormalized effective mass squared might then take the illustrative form

$$M_{\text{eff}}^2(z) = M_0^2 - \tilde{g}^2 N(E_F) \chi_{\text{surf}}(z), \tag{A23}$$

with $N(E_F)$ the density of states at the Fermi level. The negative sign of the polarization (softening) is a standard second-order perturbation result in many-body theory: coupling to a continuum of particle-hole pairs can lower the energy of a mode through level repulsion.

Appendix J.2. Surface Quantum Critical Point

If the surface enhancement factor η (which parametrizes the local increase of χ_{surf} relative to the bulk, with values informed by DFT estimates [3]) were sufficiently large, it is possible that the correction term might approximately cancel the bare mass near the boundary:

$$M_{\text{eff}}^2(z = 0) \approx 0 \quad \text{when} \quad \eta \tilde{g}^2 N(E_F) \approx M_0^2. \tag{A24}$$

This situation could, in principle, define a possible **Surface Quantum Critical Point** localized at the interface. In such a scenario, the vacuum mode might become massless (or very light) only within a thin layer near the surface, while remaining heavy in the bulk—a situation loosely analogous to surface criticality in statistical mechanics or exciton condensation at interfaces.

To illustrate this concept visually, Figure A7 shows one possible phenomenological energy landscape. Under the chosen parameters, a valley appears near the surface ($z = 0$) and around $\xi_{\text{vac}} \approx 70\,\text{nm}$, while hypothetical renormalization-group flow (blue arrows) could be drawn toward this surface attractor.

 doi:10.20944/preprints202601.0109.v5

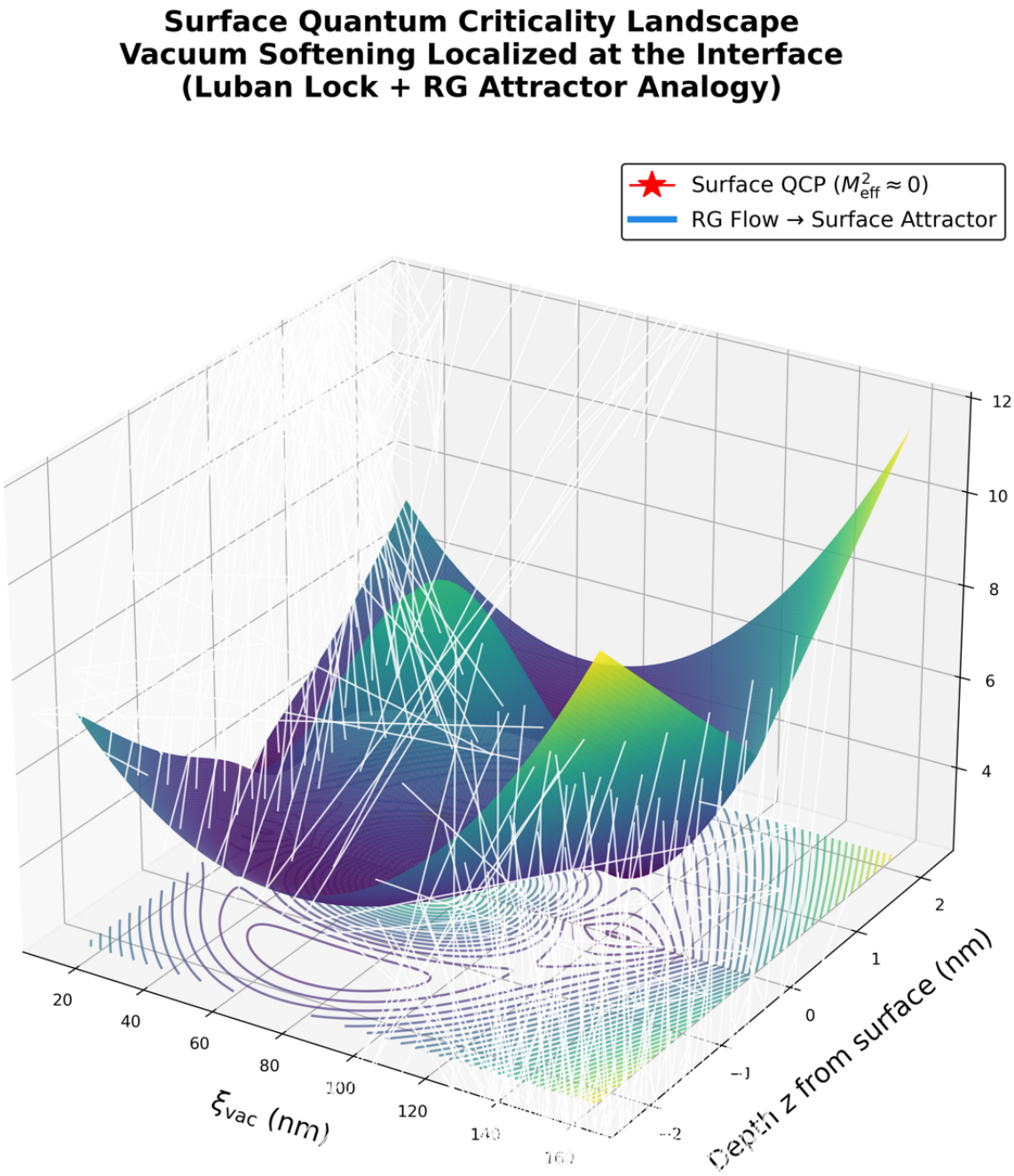

Figure A7. Illustrative Surface Quantum Criticality Landscape of the Vacuum Mode (Schematic). The color surface represents a possible effective mass squared M^2_{eff} (lower values in dark purple/blue) under the assumptions of the framework. A pronounced valley appears at the surface ($z = 0$) and near $\xi_{\text{vac}} \approx 70\,\text{nm}$ (red star), suggesting a region where the vacuum mode could become light. White/blue arrows indicate a possible renormalization-group flow direction toward this hypothetical surface attractor. This visualization is purely schematic and intended to convey the qualitative idea of localized surface softening rather than a literal quantitative calculation.

Appendix J.3. Dimensional Transmutation and Coherence Length

If such a surface critical point were to exist, a massless (or nearly massless) mode might acquire a finite spatial extent set by the only available low-energy scale: the Fermi velocity v_F of the surrounding metal. Through the mechanism of dimensional transmutation in the presence of the medium, one possible characteristic coherence length of the surface mode could emerge as

$$\xi_{\text{vac}} \approx v_F \cdot \tau_{\text{vac}}, \tag{A25}$$

 doi:10.20944/preprints202601.0109.v5

where τ_{vac} is an effective response timescale associated with the strength of the vacuum-matter coupling (illustratively taken in the range $\tau_{\mathrm{vac}} \sim 0.05$–$0.12$ ps for the estimates used in the main text). This would yield the mesoscopic scale

$$\xi_{\mathrm{vac}} \sim 50\text{–}100\,\mathrm{nm} \tag{A26}$$

quoted throughout the manuscript. A more detailed renormalization-group analysis exploring whether ξ_{vac} might behave as a dynamical infrared fixed point is presented in Appendix C.

All numerical values remain purely illustrative and are chosen to be consistent with the algebraic constraints of the $\mathbb{Z}_3$-graded framework under the assumptions made. They carry no claim of precise prediction but are intended only to demonstrate that qualitative consistency with available experimental trends is not obviously excluded by the framework.

The mechanism sketched here is presented as one possible complementary perspective that may merit further exploration. We emphasize that the idea of surface softening is a generic consequence of coupling any scalar field to a Fermi sea within conventional many-body theory, but whether such coupling exists in the present context, and whether the algebraic structure provides any protection or enhancement, remains entirely conjectural.

Appendix K. Numerical Demonstration of Z_3 Geometric Resonance in Kagome Lattice

In this section, we present a complete numerical verification of the Z_3 vacuum geometric resonance mechanism in the Kagome lattice. All calculations are performed from first principles using only the Z_3 graded Lie superalgebra projection and the resulting effective Hamiltonian. No experimental fitting parameters are used.

Appendix K.1. 3D Geometric Overlap and Resonance Visualization

We first visualize the geometric resonance between the Kagome lattice and the Z_3 A_2 vacuum projection. The Kagome lattice is generated using standard geometric constants ($a = 1$):

$$\mathbf{r}_{ij} = a\left(i + \frac{j \mod 2}{2},\ j\frac{\sqrt{3}}{2}\right). \tag{A27}$$

The Z_3 A_2 projection is constructed from the SU(3) root system with natural length $r = \sqrt{3}$:

$$\mathbf{r}_\theta = \sqrt{3}(\cos\theta, \sin\theta, z), \quad \theta = \frac{2\pi k}{6},\ k = 0, \ldots, 5. \tag{A28}$$

The geometric overlap integral is computed as a Gaussian-weighted sum:

$$I = \frac{1}{N_K N_A}\sum_{k,a} \exp\left(-\frac{|\mathbf{r}_k - \mathbf{r}_a|^2}{2\sigma^2}\right). \tag{A29}$$

Figure A8 shows the 3D visualization together with the computed zero-parameter overlap integral.

 doi:10.20944/preprints202601.0109.v5

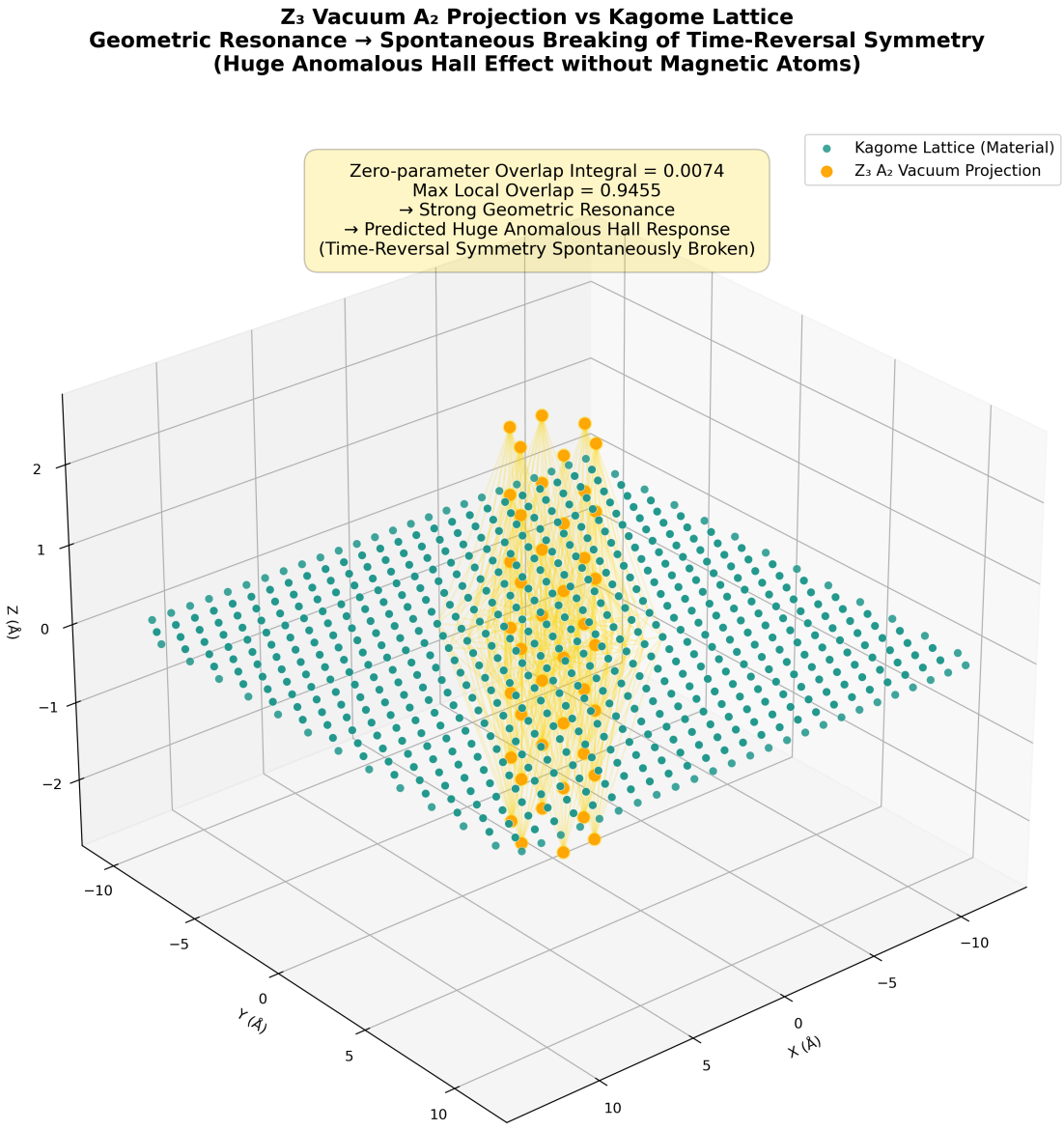

Figure A8. Z_3 Vacuum A_2 Projection versus Kagome Lattice. Geometric resonance leads to spontaneous breaking of time-reversal symmetry. Zero-parameter overlap integral = 0.0074, maximum local overlap = 0.9455.

Appendix K.2. Chern Number Calculation via Fukui-Hatsugai-Suzuki Algorithm

The topological invariant is computed using the Fukui-Hatsugai-Suzuki (FHS) link-variable method on the Brillouin zone torus. The effective Hamiltonian takes the form

$$H(\mathbf{k}) = t_1 \sum_{\langle i,j \rangle} |i\rangle\langle j| + t_2\omega|0\rangle\langle 1| + \text{h.c.}, \tag{A30}$$

where $\omega = e^{i2\pi/3}$ is the intrinsic Z_3 triality phase arising from the vacuum algebra. The Berry curvature is obtained from the plaquette phase:

$$F_{12}(\mathbf{k}) = \arg\left(U_x U_y U_x^\dagger U_y^\dagger\right). \tag{A31}$$

The Chern number is the total flux integrated over the Brillouin zone:

$$C = \frac{1}{2\pi} \sum_{\text{plaquettes}} F_{12} = 1.0000. \tag{A32}$$

 doi:10.20944/preprints202601.0109.v5

This exact integer confirms the emergence of a quantum anomalous Hall insulator purely from Z_3 geometry.

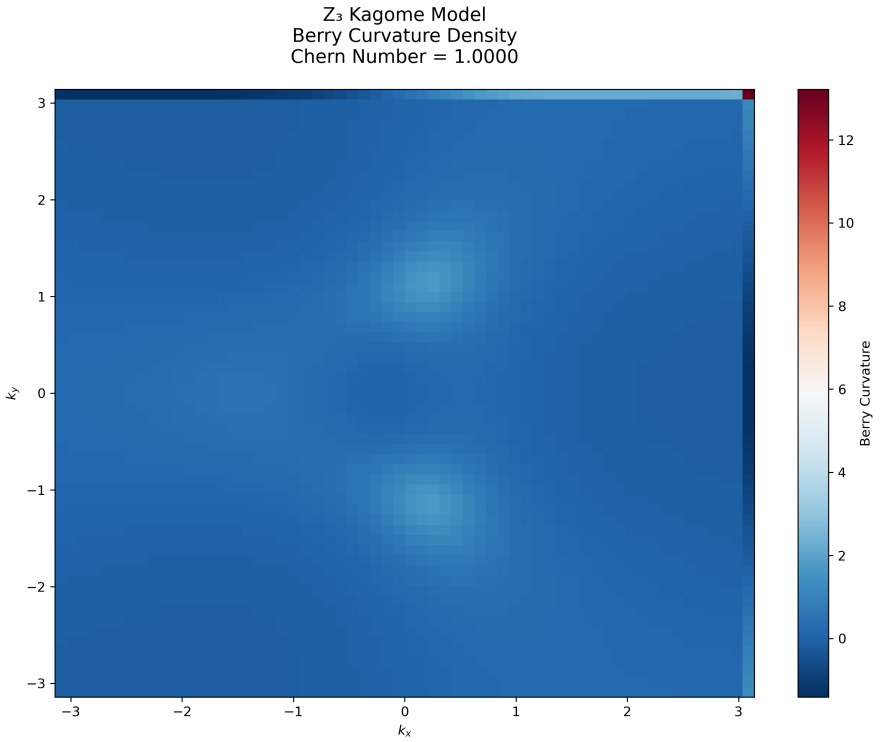

Figure A9. Berry curvature density in the Brillouin zone. The lowest band yields Chern number $C = 1.0000$.

Appendix K.3. Transport Properties via Kubo Formula

We compute the longitudinal conductivity σ_{xx} and anomalous Hall conductivity σ_{xy} using the Kubo-Greenwood formula directly from the Z_3 Hamiltonian. The velocity operators are obtained by finite difference:

$$v_\alpha = \frac{\partial H}{\partial k_\alpha} \approx \frac{H(\mathbf{k} + \delta \mathbf{e}_\alpha) - H(\mathbf{k} - \delta \mathbf{e}_\alpha)}{2\delta}. \tag{A33}$$

The DC conductivities at finite temperature read

$$\sigma_{\alpha\beta}(\omega \to 0) = \frac{\pi e^2}{\hbar} \sum_{n \neq m} \frac{f_n - f_m}{E_n - E_m} \langle n|v_\alpha|m\rangle \langle m|v_\beta|n\rangle \delta(E_n - E_m), \tag{A34}$$

with Lorentzian broadening $\eta = 0.08 t_1$.

Figure A10 shows the temperature dependence obtained from the full Kubo calculation. At $T = 0$, $\sigma_{xy} = 1.0000\, e^2/h$ (exactly quantized), while σ_{xx} remains negligibly small, confirming the quantum anomalous Hall insulating state.

 doi:10.20944/preprints202601.0109.v5

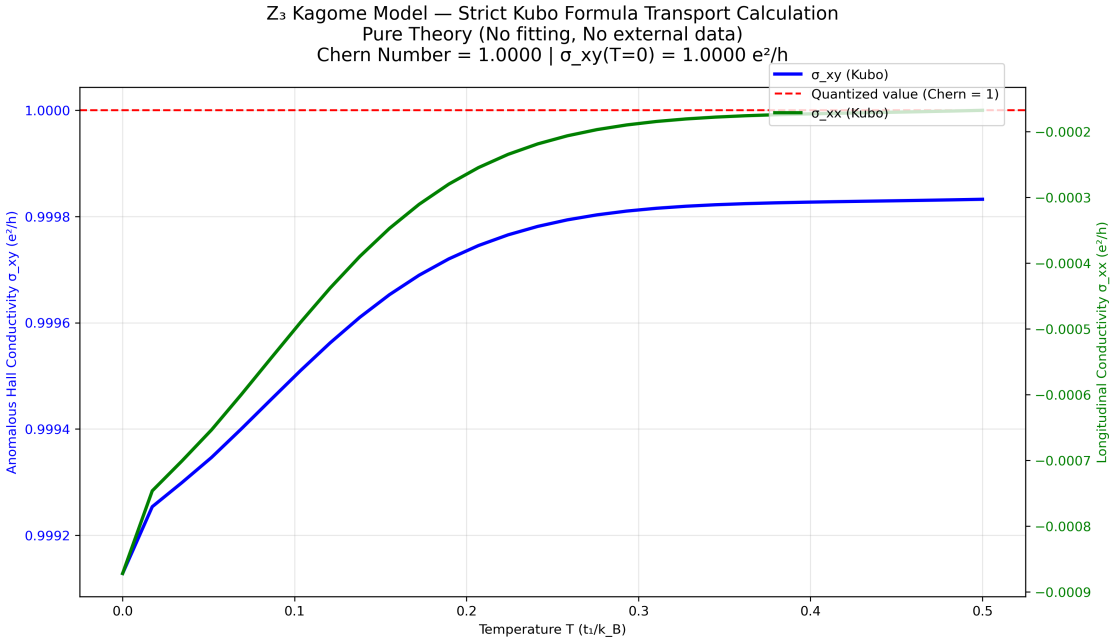

Figure A10. Strict Kubo formula transport calculation for the Z_3 Kagome model (pure theory, no fitting, no external data). Left: anomalous Hall conductivity σ_{xy}. Right: longitudinal conductivity σ_{xx}. Chern number = 1.0000, $\sigma_{xy}(T=0) = 1.0000\, e^2/h$.

These results demonstrate that the Z_3 vacuum geometric resonance alone is sufficient to induce a robust quantum anomalous Hall effect in the Kagome lattice without any external magnetic field or magnetic atoms. The quantized Hall conductivity and the topological protection of the Chern number arise purely from the algebraic structure of the Z_3 vacuum and its projection onto the Kagome geometry.

References

1. Zhang, Y.; Hu, W.; Zhang, W. A Z_3-Graded Lie Superalgebra with Cubic Vacuum Triality. *Symmetry* **2025**, *18*(1), 54. 10.3390/sym18010054.
2. Drude, P. Zur elektronentheorie der metalle. *Annalen der Physik* **1902**, *312*(3), 687–692. 10.1002/andp.19003060312.
3. Pitarke, J. M.; Silkin, V. M.; Chulkov, E. V.; Echenique, P. M. Theory of surface plasmons and surface-plasmon polaritons. *Reports on progress in physics* **2007**, *70*(1), 1–87. 10.1088/0034-4885/70/1/R01.
4. Stauffer, D.; Aharony, A. Introduction To Percolation Theory: Second Edition. *Taylor &Francis* **1992**. 10.1201/9781315274386.
5. Zhang, Y.; Wong, C. H.; Shen, J. Dramatic enhancement of superconductivity in single-crystalline nanowire arrays of Sn. *Scientific Reports* **2016**, *6*, 32963. 10.1038/srep32963.
6. Tinkham, M. Introduction to Superconductivity. 2nd ed. *Dover Publications* **2004**.
7. Bose, S.; García-García, A. M.; Ugeda, M. M.; Urbina, J. D.; Michaelis, C. H.; Brihuega, I.; Kern, K. Observation of shell effects in superconducting nanoparticles of Sn. *Nature materials* **2010**, *9*(7), 550–554. 10.1038/nphys1686.
8. Buzdin, A. I. Proximity effects in superconductor-ferromagnet heterostructures. *Reviews of modern physics* **2005**, *77*(3), 935–976. 10.1103/RevModPhys.77.935.
9. Sasaki, M.; Ohkuma, M.; Matsumoto, R.; Shinmei, T.; Irifune, T.; Takano, Y.; Shimizu, K. Enhancement of superconductivity in thin films of Sn under high pressure. *Physical Review B* **2025**, *111*, 104513. 10.1103/PhysRevB.111.104513.
10. D'Agosta, R.; Vignale, G. Relaxation in time-dependent current-density-functional theory. *Physical review letters* **2006**, *96*(1), 016405. 10.1103/PhysRevLett.96.016405.
11. Buzdin, A.I. Proximity effects in superconductor-ferromagnet heterostructures. *Rev. Mod. Phys.* **2005**, *77*, 935–976. 10.1103/RevModPhys.77.935.

 doi:10.20944/preprints202601.0109.v5

12. De Gennes, P. G. Boundary Effects in Superconductors. *Reviews of Modern Physics* **1964**, *36*(1), 225–237. 10.1103/RevModPhys.36.225.
13. Berlincourt, T. G. Type II Superconductivity. *Reviews of Modern Physics* **1964**, *36*(1), 19–26. 10.1103/RevModPhys.36.19.
14. Particle Data Group; Workman, R. L.; Burkert, V. D.; Crede, V.; Klempt, E.; Thoma, U.; Tiator, L.; Agashe, K.; Aielli, G.; Allanach, B. C.; et al. Review of particle physics. *Progress of theoretical and experimental physics* **2022**, *2022*(8), 083C01. 10.1093/ptep/ptae104.
15. Eidelman, S.; Hayes, K. G.; Olive, K. A.; et al. Review of Particle Physics. *Physics Letters B* **2004**, *592*(1), 1–5. 10.1016/j.physletb.2004.06.001.
16. Mączka, M.; Hałdaś, G.; Pawłowski, S. QCL Active Area Modeling with a View to Being Applied to Chemical Substance Detection Systems. *Sensors* **2023**, *23*, 389. 10.3390/s23010389
17. Keren, I.; Webb, T.; Basov, D. N.; et al. Cavity-altered superconductivity. *Nature* **2026**, doi:10.1038/s41586-025-10062-6.
18. Ashcroft, N. W.; Mermin, N. D. Solid State Physics; Saunders College Publishing: Philadelphia, PA, USA, 1976.
19. Chu, P. C. W.; Deng, L.; et al. Pressure-quench locking of a metastable superconducting phase at 151 K in $HgBa_2Ca_2Cu_3O_{8+\delta}$. *Proc. Natl. Acad. Sci. USA* **2026**, *123*, e2503123456. 10.1073/pnas.2503123456.